

SOL-GEL DEPOSITION OF BaTiO₃ THIN FILMS FOR ELECTRO-
OPTIC WAVEGUIDE MODULATORS

BY

DAVID KEITH BOWMAN

A THESIS
SUBMITTED TO THE FACULTY OF

ALFRED UNIVERSITY

IN PARTIAL FULFILLMENT OF THE REQUIREMENTS
FOR THE DEGREE OF

MASTER OF SCIENCE

IN

CERAMIC ENGINEERING

ALFRED, NEW YORK

SEPTEMBER, 2004

Alfred University theses are copyright protected and may be used for education or personal research only. Reproduction or distribution in part or whole is prohibited without written permission from the author.

SOL-GEL DEPOSITION OF BaTiO₃ THIN FILMS FOR ELECTRO-
OPTIC WAVEGUIDE MODULATORS

BY

DAVID KEITH BOWMAN

B.S. ALFRED UNIVERSITY (2002)

SIGNATURE OF AUTHOR _____ (Signature on file)

APPROVED BY _____ (Signature on file)

SUHAS BHANDARKER, ADVISOR

(Signature on file)

WALTER SCHULZE, ADVISORY COMMITTEE

(Signature on file)

STEVE PILGRIM, ADVISORY COMMITTEE

(Signature on file)

DOREEN EDWARDS, CHAIR, ORAL THESIS DEFENSE

ACCEPTED BY _____ (Signature on file)

ALASTAIR CORMACK, DEAN,
SCHOOL OF ENGINEERING

ACKNOWLEDGMENTS

I would like to extend my most profound gratitude to the following people:

My advisor, Dr. Suhas Bhandarkar, for his direction and advice these past semesters.

My committee, Drs. Steven Pilgrim and Walter Schulze, for their guidance and constant concern for my success as a student and a ceramist over the past 6 years.

My collaborator, Dr. Glen Kowach, for his hospitality and his enlightening conversation.

Fran Williams, Steve Conderman and Swavek Zdziezinski, for their patience and assistance with the laboratory equipment.

Pat LaCourse, Beverly Crowell and Mercedes Hanbach, for their aid in gathering resources and reviewing this manuscript.

All of my friends, and the friends of 2 Mill Street, for making these past two years what everyone's college experience should be like.

My family, for their unending love and support. My success is a testament to them.

TABLE OF CONTENTS

	Page
Acknowledgments	iii
Table of Contents.....	iv
List of Tables.....	v
List of Figures.....	vi
Abstract	ix
I INTRODUCTION.....	1
A. Overview	1
B. Mach-Zehnder Waveguide Modulators	3
C. Brief Introduction to Non-linear Optics.....	4
D. Electro-optic Materials	7
E. Thin Film Deposition	8
F. Sol-gel Deposition.....	12
II EXPERIMENTAL PROCEDURE.....	14
A. Theory of Prism Coupling	14
B. Sol-gel Preparation and Deposition.....	22
C. Thin Film Characterization	24
III RESULTS AND DISCUSSION	26
A. Substrate Characterization	26
B. Sol Preparation and Characterization	27
C. Effect of Spin Coating Parameters on Film Properties.....	29
D. Effect of Heating Rate on Film Properties.....	34
E. Effect of Insertion Temperature on Film Properties.....	43
F. Effect of Insertion Temperature on Waveguide Loss.....	56
G. Proposed Mechanisms	63
IV SUMMARY AND CONCLUSIONS.....	66
V FUTURE WORK	68
REFERENCES	71

LIST OF TABLES

	Page
Table I. Electro-optic Properties of Some Ferroelectric Materials	8
Table II. Typical Measurement Capabilities of Metricon P-1 Prism at 633 nm	14
Table III. Prism Coupling Data Collected from Gel Films	32
Table IV. Optical Properties and Crystallite Size of Fired Films	56

LIST OF FIGURES

	Page
Figure I.1. Optical communications transmission link.....	1
Figure I.2. Mach-Zehnder Waveguide Modulator.	3
Figure I.3. Monomer of polyvinylpyrrolidone.....	13
Figure II.1. Schematic of prism coupling measurement setup.....	16
Figure II.2. Photograph of prism coupling measurement setup.	16
Figure II.3. Peaks in reflected intensity corresponding to guiding modes, as measured by a prism coupler.	17
Figure II.4. Photograph of waveguide loss measurement setup.....	21
Figure II.5. Exponential curve corresponding to waveguide loss, as measured by a prism coupler.	22
Figure II.6. Specialty Coating Systems Model G3-8 Desktop Precision Spin Coating System, Cookson Electronics.	24
Figure III.1. Prism coupling spectrum of silica thermal oxide on silicon wafer.	27
Figure III.2. Simultaneous DSC-TGA of barium titanium alkoxide sol.	28
Figure III.3. Prism coupling spectrum of gel film spun coat at 2000 rpm.	30
Figure III.4. Prism coupling spectrum of gel film spun coat at 1500 rpm.	30
Figure III.5. Prism coupling spectrum of gel film spun coat at 1000 rpm.	31
Figure III.6. Prism coupling spectrum of gel film spun coat at 500 rpm.	31
Figure III.7. Thickness of gel films as a function of spinning speed. (Note: Error bars obscured by marker.).....	32

Figure III.8.	Thermal cycles for samples 1-4, showing different heating rates.....	35
Figure III.9.	Prism coupling spectrum of sample heated at 5K/minute.	36
Figure III.10.	Prism coupling spectrum of sample heated at 10K/minute.	36
Figure III.11.	Prism coupling spectrum of sample heated at 0.5K/minute from 300°C to 500°C.	37
Figure III.12.	Prism coupling spectrum of sample step heated to temperature.....	37
Figure III.13.	Effective index of TE ₀ as a function of firing time.	39
Figure III.14.	X-ray diffraction pattern of sample heated at 5K/minute; crystallite size, 196Å. (BaTiO ₃ peak lines included)	40
Figure III.15.	X-ray diffraction pattern of sample heated at 10K/minute; crystallite size, 181Å.	40
Figure III.16.	X-ray diffraction pattern of sample heated at 0.5K/minute from 300°C to 500°C; crystallite size, 260Å.	41
Figure III.17.	X-ray diffraction pattern of sample step heated to temperature; crystallite size, 173Å.	41
Figure III.18.	Crystal size as a function of time at elevated temperature.	43
Figure III.19.	Prism coupling spectra of samples spun cast at 2000rpm.	44
Figure III.20.	Prism coupling spectra of samples spun cast at 1500rpm.	45
Figure III.21.	Prism coupling spectra of samples spun cast at 1000rpm.	46
Figure III.22.	Prism coupling spectra of samples spun cast at 500rpm.	47
Figure III.23.	Film thickness as a function of insertion temperature.....	49
Figure III.24.	Film refractive index as a function of insertion temperature.....	50
Figure III.25.	Film refractive index as a function of film thickness.	50

Figure III.26. X-ray diffraction pattern of sample spun coat at 2000 rpm and heated to 500°C.....	52
Figure III.27. X-ray diffraction pattern of sample spun coat at 2000 rpm and heated to 700°C.....	52
Figure III.28. Prism coupling spectrum of sample spun coat at 2000 rpm and heated to 500°C then 700°C, TE/TM.	54
Figure III.29. Prism coupling spectrum of sample spun coat at 2000 rpm and heated to 300°C, 500°C and 700°C.	54
Figure III.30. X-ray diffraction pattern of sample spun coat at 2000 rpm and heated to 500°C then 700°C.....	55
Figure III.31. X-ray diffraction pattern of sample spun coat at 2000 rpm and heated to 300°C, 500°C and 700°C.	55
Figure III.32. Waveguide loss of sample spun coat at 2000 rpm and heated to 80°C; approximately 1 dB/cm.	57
Figure III.33. Waveguide loss of sample spun coat at 2000 rpm and heated to 220°C; approximately 1.5 dB/cm.....	58
Figure III.34. Waveguide loss of sample spun coat at 2000 rpm and heated to 270°C; approximately 3 dB/cm.....	58
Figure III.35. Waveguide loss of sample spun coat at 2000 rpm and heated to 320°C; approximately 15 dB/cm.....	59
Figure III.36. Waveguide loss of film as a function of insertion temperature.	60

ABSTRACT

Barium titanate thin films were deposited onto silica-clad silicon using a sol-gel spin coating process. Such films could have valuable applications as electro-optic waveguide components and devices. A large polymer, polyvinylpyrrolidone, was added to a conventional acetate-based sol-gel to increase film thickness. The effect of processing parameters on thin film properties was studied using several techniques including prism coupling. This method also was used to study the optical loss in the films. The films were heat-treated under various conditions and a rapid heating recipe (fast ramp to 500°C then 700°C for 30 minutes) was shown to fully crystallize the film to perovskite BaTiO₃. The as deposited films show desirably low loss (~1 dB/cm). However, the loss in all the fired films was very high despite the fact that the grain size in the film is on the order of 10-20nm. The results indicated that this high loss was locked into the system early during the organic removal phase, which was unexpected. Pyrolysis of the large polymeric molecules can be expected to create a new structure within the porous film consisting of isolated, but interconnected nanodomains of solid. A mechanism is proposed where clusters of the domains scatter light in the pyrolyzed films. This phenomenon evidently continues to dominate all the way to the final densified polycrystalline state.

I INTRODUCTION

A. Overview

The recent burgeoning growth in digital communication, driven by the advent of consumer Internet, has led to the need for faster data transmission systems. Future optical communications systems will soon require high-speed photonic components capable of speeds in excess of 100 Gbps. Such systems will only be possible through significant enhancements of the individual components both in terms of their cost and performance.

A simplified version of the typical communications system is shown in Figure I.1.

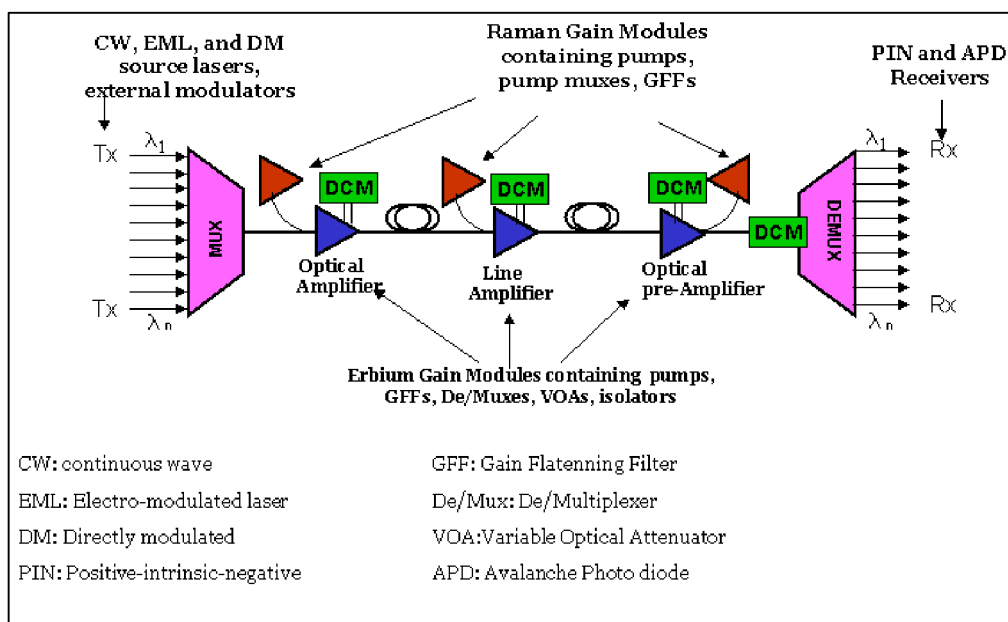


Figure I.1. Optical communications transmission link.

The four main sub-systems are the source, the optical fiber, the amplifiers and the detector. The optical fiber acts as the pipeline for the optical signal generated by the source. These fibers operate as dielectric waveguides in total internal reflection (TIR) mode. For long haul applications, the loss in the fiber necessitates signal amplification at periodic points in the link. Traditional amplifiers would convert the optical signal to an electrical one, then amplify it and finally convert it back to optical. Modern amplifiers can accomplish this ‘all-optically’ using erbium-doped fiber for signals at and around 1550 nm, the lowest loss region for typical silica fibers. At the receiving end, the detector system is commonly composed of an array of photodetectors, such as PIN-diodes or avalanche photodiodes.

At the source, the two most important components are the light generation device and the device to convert the electronic data to a digital optical signal. There are typically several options for optical signal generation: direct modulation, electro-absorption modulation and phase modulation. Direct modulation involves simply turning the laser on and off to transform the electrical signal to the corresponding optical bits. This works well for low speed transmission (<2.5 Gbps), but generates significant chirp in the signal at higher speeds. In contrast, an externally modulated system uses a continuous wave (CW) laser and a separate optoelectronic device to convert the electrical signal to an optical one. One option for a device for external modulation is the electro-absorption modulator, which makes use of the Franz-Keldysh effect.¹ Alternatively, an electro-optic phase modulator that uses the Pockels or Kerr effect to switch the signal can be used and is the preferred device.²

B. Mach-Zehnder Waveguide Modulators

Such a modulator is based on the electro-optic effect seen in LiNbO_3 and often uses the Mach-Zehnder interferometer design. These modulators, capable of operation at speeds up to 40 Gbps (for the on-coming OC768 systems) and requiring only a few volts to switch, are now commercially available.³

A Mach-Zehnder waveguide modulator, shown in Figure I.2, takes a continuous lightwave and splits it into two beams using a Y-junction or a 3dB coupler. At the other end of the device, the beams recombine. The light is modulated in the device by means of the Pockels effect of the waveguide material. This effect has been used to make high-speed switches and could also lead to novel future devices such as wavelength converters, electrically tunable gratings or for optical storage.

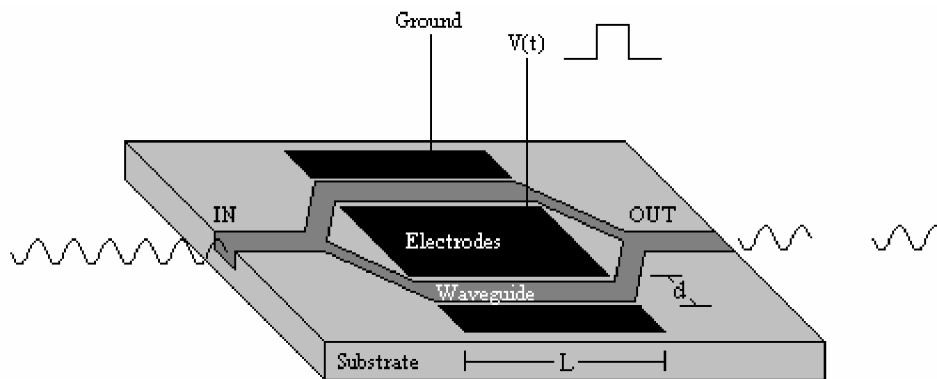


Figure I.2. Mach-Zehnder Waveguide Modulator.

C. Brief Introduction to Non-linear Optics

Since light is an electro-magnetic radiation, its interaction while propagating through a non-magnetic dielectric media is described by the polarizability of the medium. The linear relationship between displacement D , electrical field E and polarization P is given as:

$$D = \epsilon_0 E + P \quad (1)$$

where ϵ_0 is the permittivity of free space. The polarization term takes into account the material response to the electrical field:

$$P = \epsilon_0 \chi E \quad (2)$$

where χ is the linear dielectric susceptibility of the material. By combining terms we may define the material permittivity:

$$\epsilon = \epsilon_0 (1 + \chi) \quad (3)$$

For real materials, polarization can be expressed as a series of higher order susceptibilities:

$$P = \epsilon_0 \chi E + \epsilon_0 \chi' E^2 + \epsilon_0 \chi'' E^3 \quad (4)$$

where χ' and χ'' are the second and third-order non-linear susceptibilities. The terms of yet higher order turn out to be small enough in value to be insignificant. In fact, most materials behave linearly so that even χ' and χ'' are negligibly small.

If one were to expand the response of the index of refraction to electrical field, similar to polarizability above, the relevant terms would be:

$$n = n_0 + a_1 E + a_2 E^2 \quad (5)$$

where a_1 and a_2 are the first and second order electro-optic effect coefficients. The linear dependence of index of refraction to electrical field is related to the second-order non-linear susceptibility and the quadratic dependence, to the third order non-linear coefficient. Only noncentrosymmetric materials (crystal lattices with no center of symmetry) display second order non-linearity, while all materials show at least some third order non-linear behavior. The Pockels effect is a special case of the second order non-linear behavior and is commonly used in electro-optic devices. The Pockels effect is given by:

$$\Delta n = a_1 E = \frac{1}{2} n^3 r E \quad (6)$$

where r is called the Pockels coefficient. Real materials typically have coefficients in the range of 1-100 pm/V. In a Mach-Zehnder waveguide modulator, this index change manifests itself as a phase difference, $\Delta\phi$, in the optical wave traveling through the two branches:

$$\Delta\phi = \left(\frac{2\pi}{\lambda}\right) n^3 r \left(\frac{L}{d}\right) V \quad (7)$$

where L and d are the length and separation distance of the electrodes respectively and V is the applied voltage. Should no bias be placed across the device, constructive interference of the light upon recombination would produce the "on" state. If a characteristic potential - called the half-wave voltage, V_π - were placed across one of the two arms as light passes through it, the resultant π phase shift would cause destructive interference and a null or "off", output signal.

The current incarnation of a waveguide modulator is a modified LiNbO₃ crystal package. A boule of the single crystal is grown using a flux method. The boule is cut with a diamond saw and the faces are lapped parallel then polished to an optical finish. This is similar to the treatment a silicon wafer gets during production. A thin strip of titanium is diffused into the substrate to create a path of higher index of refraction. This index change is sufficient to confine the light. The crystals are cut to shape, electrodes are evaporated onto the surface, optic fiber leads are affixed and the device is packaged in a metal casing. These waveguide modulator packages are small, modular and capable of operation at 1550 nm with switching speeds efficient up to 40 GHz.³

D. Electro-optic Materials

Many members of the ferroelectric material class have been shown to have significant electro-optic coefficients, in particular LiNbO_3 , $\text{Pb}_{1-x}\text{La}_x\text{Zr}_{1-y}\text{Ti}_y\text{O}_3$ (PLZT) and BaTiO_3 .⁴ These are the preferred materials due to their excellent stability and reliability. The same goes for more exotic materials such as tungsten-bronze strontium barium niobate. While LiNbO_3 has been a favorite of the industry for some time, other ferroelectric materials have also been intensely investigated for this application. BaTiO_3 is a prime candidate for electro-optic devices because both its r -coefficient and the n^3r figure of merit are the highest in its material class.⁵ PLZT has drawn considerable attention in the optical community since the 1970's due to its transparency in the visible spectrum and high electro-optic coefficient.⁶ The grain boundary structure of fully dense BaTiO_3 or PLZT is feared to be too scattering for use as a waveguide.⁵ However, growing single crystals of these materials is very difficult and it takes an unacceptably long time to grow one of suitable scale for waveguide devices.⁷ Thus lithium niobate has remained the material of choice to date due to the relative ease of single crystal growth and its acceptable electro-optical properties.

Despite having electro-optic coefficients almost two orders of magnitude lower than barium titanate, its smaller low-frequency dielectric constant makes lithium niobate an attractive material. Table I shows some examples of electro-optic properties of these materials.^{5,6} As shown previously, an important figure of merit in switching applications is n^3r . This number is directly related to the induced birefringence of the material.

Table I. Electro-optic Properties of Some Ferroelectric Materials

Material	r (pm/V)	n	n ³ r (pm/V)
BaTiO ₃	1,640	2.46	24,400
Sr _{0.75} Ba _{0.25} Nb ₂ O ₆	1,340	2.30	16,303
Pb _{0.91} La _{0.09} Zr _{0.65} Ti _{0.35} O ₃	612	2.50	9,563
LiNbO ₃	32	2.27	374

E. Thin Film Deposition

In order to use these strongly non-linear materials for electro-optic switching, the alternative to bulk materials and single crystals is thin films. Thin film deposition of these ferroelectrics holds the added appeal of integrated optics. The long cherished goal in photonics has been the integration of active components with passive circuitry. Waveguides made of silica on silicon can be used to make light-guiding patterns capable of directing, splitting and coupling light. Amplification of light in these waveguides at the 1550 nm wavelength has also been achieved using erbium doping. Thermo-optic switching has been well implemented with planar lightwave circuits and is the only present mode of controlling the light path. The electro-optic effect in waveguides is coveted but limited solely to LiNbO₃ which severely limits the integration possibilities. Thin film waveguide modulators would be a valuable addition to the capability of planar lightwave circuits (PLC's), which is the driving force for this work.

Scattering is the biggest concern associated with a polycrystalline microstructure. To avoid this scattering, it is desirable to have grains smaller than the wavelength of

light. That way, grain boundaries would scatter less and dielectric mismatch between grains would be minimized.^{8,9}

Thin film deposition of electro-optic materials has been rigorously studied by many methods. The majority of the literature on this subject focuses on vacuum techniques such as Pulsed Laser Deposition (PLD), Chemical Vapor Deposition (CVD), Radio Frequency Magnetron Sputtering and Molecular Beam Epitaxy (MBE).¹⁰ Thin film barium titanate was reported as being grown on an MgO substrate using MBE in the early nineties.¹¹ Loss lower than 1 dB/cm was reported at the HeNe wavelength in BaTiO₃ films.

Buchal et al. have been successful in using PLD to craft barium titanate films (and subsequently waveguides) on MgO substrates.¹² Research has also been conducted on MgO buffer layers on various substrates.¹³⁻¹⁵ They have reported propagation losses as low as 1-2 dB/cm at both the HeNe and 1.55 micrometer wavelengths and have achieved switching speeds up to 1 MHz.¹⁶ Several other researchers have reported on barium titanate or strontium barium titanate films deposited using PLD, but have not fabricated devices or published waveguide properties.¹⁷⁻²³

Wessels et al. have been investigating metal-oxide CVD for some years now as a deposition technique.²⁴ They have reported textured growth of barium titanate films on MgO substrates and MgO-buffered silicon.²⁵ They have also successfully developed waveguide modulators for operation at both the 1.55 and 1.31 micrometer wavelengths with losses of 4 ± 2 dB/cm.²⁶ More recently, they have succeeded in doping their CVD films with erbium and have reported gains at 1.55 μm of 3 dB/cm.²⁷⁻²⁹

Kim and Hishita have been studying barium titanate films deposited using RF Magnetron sputtering.³⁰⁻³² They report the use of MgO substrates as well as on MgO-buffered silicon to template the growth of epitaxial films. Barrios, et al. at the University of Pittsburgh report incorporating erbium into epitaxial barium titanate films.³³ Neither group has reported on a device or waveguide properties. It must be mentioned that there is a significant body of literature on barium titanate sputtered onto silicon or 'platinized' (Pt coated Si) silicon for non-optical applications over the past 15 years.

In addition to these vacuum techniques, there is a large amount of work in the literature dealing with sol-gel.³⁴⁻⁴³ Chemical solution deposition holds some key benefits over the more complex vacuum techniques, such as:

- 1.) The processing of the film is considerably simplified. A sputtering chamber requires many systems –vacuum pumps, cooling water, electrical heaters, RF generator, gas flow controllers, etc. - running simultaneously. Each of these subsystems is individually complex and will have a great impact on the final product. The sol-gel processing conducted in this work required only common equipment such as a furnace, a spin coater and traditional labware.
- 2.) The second key benefit is the close control that can be exerted over the composition of multiple cation systems. A vapor phase technique, such as PLD, would have to take into consideration the differential affinity of the source laser to each material in the target. One phase or material may be more susceptible to the specific energy of the laser. For example, in PLZT the volatility of lead and the refractory nature of zirconia affect the plume dynamics and the stoichiometry of the resultant film may not resemble that of

the target. A wet chemical method solves this problem by complexing the cations with organic ligands so that cation ratios can be controlled very closely.

- 3.) The third benefit is the relatively low capital expenditure. To build a sol-gel deposition process requires far less money than the equipment necessary for MBE. Overhead is enormous for MBE and the source materials are expensive.

These benefits come at the expense of liquid systems with complex chemistry.

The subtleties of preparation of the sol can have a great impact on the sol's useful lifetime, viscosity and homogeneity. By merely changing the order components are added one can sometimes change the end product. The organic species in the recipe help control the formation of the gel film and therefore the final ceramic microstructure. There are numerous recipes in the literature, each one using a different ligand or combination of solvents.¹⁰

There is also the drawback of the limited film thickness. A typical sol-gel film provides a thickness on the order of 100 nm, which is unsuitable here and in many other applications. To effectively confine light, a device would require a waveguide close to a micrometer in thickness. To this end, sol-gel thin film processes require many iterations of the deposition (often followed by pyrolysis) process. An optimized process would be able to deposit a film and sinter it to sufficient thickness in a single casting.

F. Sol-gel Deposition

Deposition of the films is performed using either a spin coater or a dip coater. These instruments evenly distribute the sol over the surface of the substrate and allow the operator some degree of control over the film thickness. The film is then subjected to an appropriate thermal treatment. The gel film is dried at room temperature, removing the solvent. It is typical to heat the film to temperatures between 300°C and 500°C to pyrolyze organics. It is at this point that the deposition process is repeated to make a thicker film. Finally, the film is heated to 700°C or higher to crystallize the ceramic. In the literature, heat treatment recipes for the films have been as widely variable as those for the sol chemistry.

The particular recipe used in this work was reported by Kozuka, et al.⁴⁴ It uses standard barium and titanium precursors, but also a polymeric additive, polyvinylpyrrolidone, whose structure is shown in Figure I.3. Kozuka et al. have shown that the pyrrolidone side-group of this large polymer chain (MW=630,000) interacts with condensation sites in the gel network, thereby restricting the gelling process. A loosely networked film can better relax during the compressive drying phase and hence greater film thicknesses, on the order of a micrometer, can be achieved.⁴⁵ The authors also describe the pyrolysis process during heat treatment using infrared spectroscopy and differential scanning calorimetry. They characterized the final sintered films with X-ray diffraction and UV-visible spectroscopy, but did not measure light-guiding properties of the film.⁴⁶

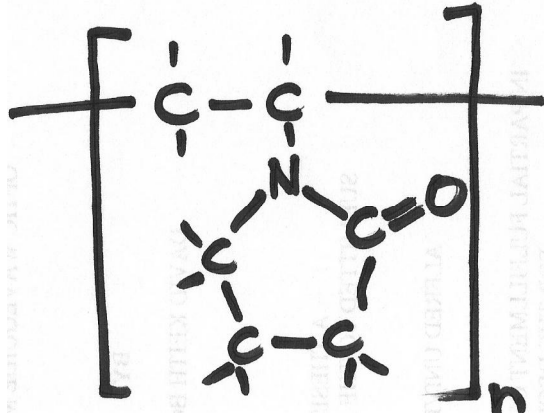


Figure I.3. Monomer of polyvinylpyrrolidone

This process was selected for study due to the reported advantage of forming thicker films and the goal of this work was to understand the interplay between the various film properties as controlled by the processing conditions and the lightguiding abilities of the final film.

II EXPERIMENTAL PROCEDURE

A. Theory of Prism Coupling

The primary characterization method used in this study was prism coupling. This method allows the measurement of film thickness and index in a single test. Owing to the nature of the measurement, the waveguide loss can also be readily measured with little alteration of the equipment set-up.

A Metricon 2010 Prism Coupler equipped with a Helium-Neon laser (633 nm) and a high index TiO₂ prism ($n_p = 1.9646$) was used to couple light into the samples. The measurement capabilities of this prism are given in Table II.

Table II. Typical Measurement Capabilities of Metricon P-1 Prism at 633 nm

Material	Index	Minimum Thickness
Silicon Dioxide	1.46	480 nm
Photoresist	1.63	420 nm
Silicon Oxy-Nitride	1.80	340 nm

The thin film sample is brought into contact with the base of a prism by means of a pneumatic coupling head, shown in Figures II.1-2. A laser of known wavelength is focused onto the face of the prism so that the ray propagates to the back face of the prism where the sample is coupled. Under normal circumstances, the light is reflected off the back face of the prism and is directed into a germanium detector. The coupling head, sample and photodetector are all mounted onto a stage that rotates about the position of the coupling spot. This allows the detector to scan a range of incident angles, thus a

range of effective indices. The effective index of the prism N_m is related to the incident angle θ by the equation:

$$N_m = n_p \sin \theta_m \quad (8)$$

where the subscript m corresponds to one of the fundamental guiding modes of the film and n_p is the index of the prism. The detected intensity is plotted as a function of angle θ and a profile similar to the one shown in Figure II.3 is obtained. The sharp dips in reflected intensity correspond to the light coupling into the film at the base of the prism due to frustrated total internal reflection (FTIR). The effective index, and therefore the angular position, at which this coupling to the guiding modes occurs is a function of many variables: mode order, film thickness, film index of refraction and absorption, index of refraction for the medium and substrate, and the polarization state of the incident light, respectively:

$$N_m = N(m, T, n, k, n_0, n_2, \rho) \quad (9)$$

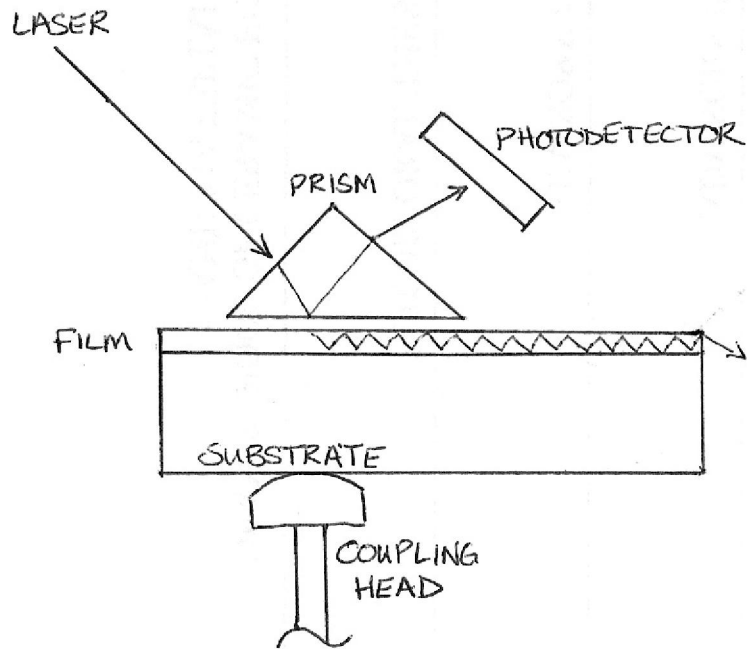


Figure II.1. Schematic of prism coupling measurement setup.

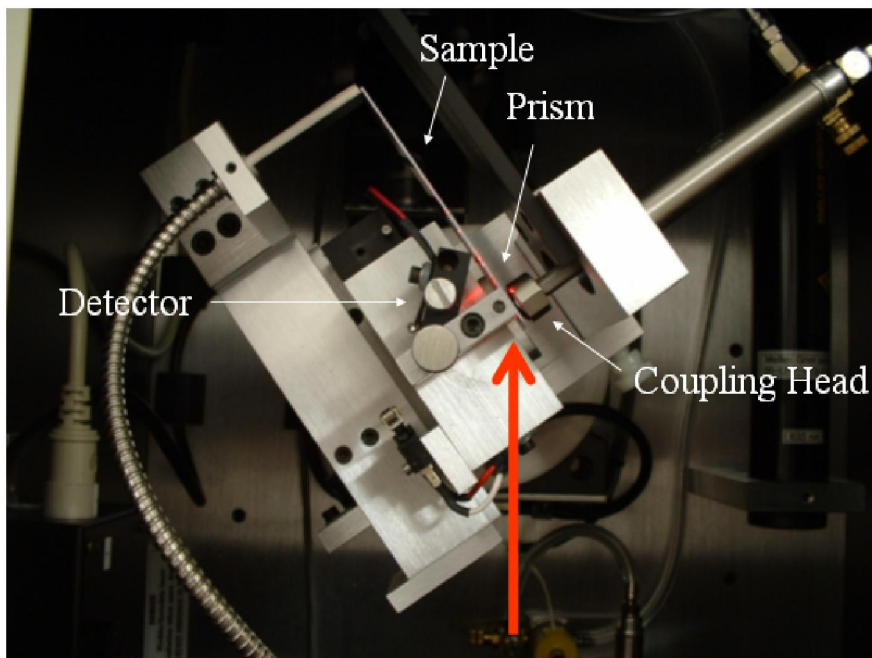


Figure II.2. Photograph of prism coupling measurement setup.

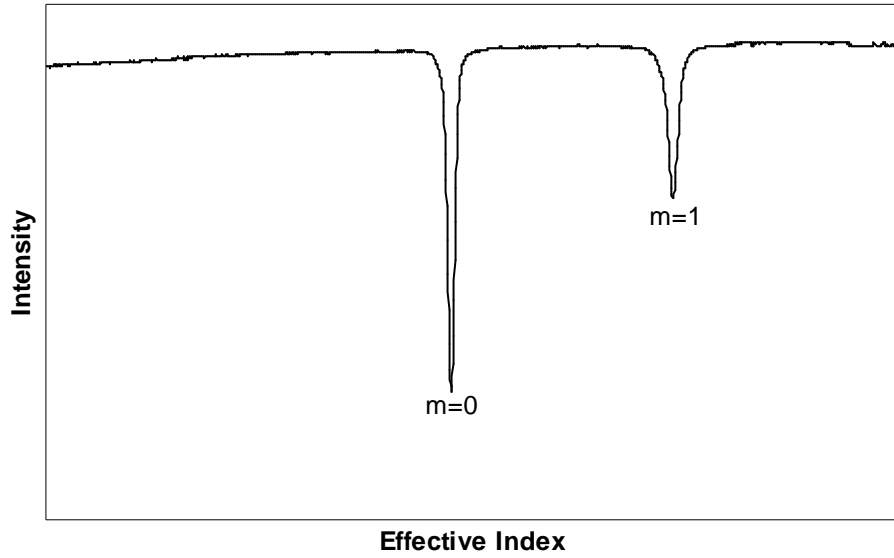


Figure II.3. Peaks in reflected intensity corresponding to guiding modes, as measured by a prism coupler.

For a typical experiment, where polarization state ($\rho=0$ for TE, $\rho=1$ for TM) and substrate index is known, the fundamental guide modes will depend only film thickness and index. This relationship is known as the waveguide equation⁴⁷:

$$kT\sqrt{n^2 - N_m^2} = m\pi + \phi_0 + \phi_2 \quad (10)$$

where k is the wavenumber ($2\pi/\lambda$) and the Fresnel phase shifts ϕ are given by:

$$\phi_j = \arctan \left\{ \left[\left(\frac{n}{n_j} \right)^{2\rho} \left[\frac{(N_m^2 - n_j^2)}{(n^2 - N_m^2)} \right] \right]^{1/2} \right\} \quad (11)$$

where $j=0$ for the film-air surface and $j=2$ for the film-substrate surface.

The two unknowns (n, T) require a minimum of two modes to be measured for simultaneous solution. In the case where only two modes are measured ($m=0,1$) the two equations can be solved together by eliminating the kT term first, and rewriting as:

$$n^2 = \frac{[(N^2_{m=0})(RHS^2_{m=1}) - (N^2_{m=1})(RHS^2_{m=0})]}{[(RHS^2_{m=1}) - (RHS^2_{m=0})]} \quad (12)$$

where ‘RHS’ represents the entire right hand side of the waveguide equation (10). This is a complex, transcendental equation that cannot be solved explicitly for n^2 , but must be calculated by a numerical convergence⁴⁷:

$$n^2_{[q]} = f(n^2_{[q-1]}) \quad (\text{for } q=1,2,3\dots\text{etc.}) \quad (13)$$

After 10-20 iterations of this calculation the error in n^2 is less than 10^{-6} and the value is suitably accurate. Once the film index of refraction is calculated, thickness can be solved by substituting the calculated value for n back into the original equation.

If more than two modes can be detected they can be used to create a least squares regression and obtain descriptive statistics for film index and thickness. There are several other important equipment parameters to consider in making a good measurement. Because the film is being physically contacted to the base of the prism the pressure at which the pneumatic arm is operating becomes an important consideration. Too high a coupling pressure will distort the film at the base of the prism and lead to broadening or

shifting of the peaks. Too low a coupling pressure and the air gap between the base of the prism and the film will be too great to support FTIR. This also becomes a problem if the surface roughness of the specimen is too high to gain an adequate coupling to the prism.

In the event that only a single peak is detected in TE mode, a second measurement using the TM mode can be made. The two peaks can then be used to calculate both index and thickness. Many of the samples fired to higher temperatures required use of this measurement option. One of the considerations that must be made when making this calculation is the crystalline direction. Although there is no dependence of thickness on the polarization state of light, there may be some dependence of the refractive index (Equation 10). The polarization state affects the right hand side of the equation, thereby changing the value of the ρ exponent. If the refractive index of the film is different in either direction, this adds a third unknown to the waveguide equation. Therefore, in a single crystal or a highly textured material, the effective index of a TM mode contains the artifact of the 'extraordinary' TM index. The X-ray diffraction data collected on these films reflects a randomly-oriented polycrystalline microstructure. Therefore, it is assumed that the bulk index of the material is unaffected by the polarization state of the incident light. This allows the simultaneous solution of two equations for the index and thickness using the two polarization states.

Since a single parameter is being measured during this experiment, angle θ , a certain degree of precision is required to gain a worthwhile result, typically less than 1 arc minute. The higher resolution mode of operation for this particular machine is 0.45 arc minutes, capable of effective index resolution of 0.0001. The light source must be

linearly polarized so that the cross-section of the laser is either TE (transverse electrical field) or TM (magnetic). Typical operation is in TE mode, where the electrical field component oscillates perpendicular to the direction of propagation. Finally, the index of the prism must be chosen so a suitable range of effective index may be measured thus encompassing as many fundamental guiding modes as possible.

The most important property of the film to optimize, i.e. minimize, is waveguide loss. As light propagates through a guiding mode down the length of the film, a fraction of the intensity is scattered. This light is detected and used to model the waveguide loss. The loss measurement is based on a scanning fiber method, as shown in Figure II.4. The stage is positioned so that the fundamental guiding mode of the sample is excited and the flow of light through the sample is maximized. The result is a propagation streak, often visible, down the length of the sample. An InGaAs fiber bundle detector is scanned down the length of this streak and light scattered from the sample is detected. This method is similar in operation to that of a CCD camera. Some appreciable amount of scattering loss is required to detect the propagation attenuation. In the absence of scratches, particles and excessive surface roughness, the attenuation will be exponential in nature, as shown in Figure II.5. The decay is modeled using a natural logarithmic function:

$$\ln(I) = (\text{intercept}) - (\text{slope})x \quad (14)$$

The loss in decibels per centimeter can be calculated using the slope of this curve:

$$Loss(dB/cm) = -10\text{Log}[e^{(slope)}] \quad (15)$$

Repeatability of this measurement is strongly dependent on the exponential behavior of the trace, usually to +/- 10%. Accuracy of the measurement is still a questionable entity as there is not yet a well-defined standardization procedure for this method. However, a well-behaved exponential curve would appear to reflect accurate measurement of decay.

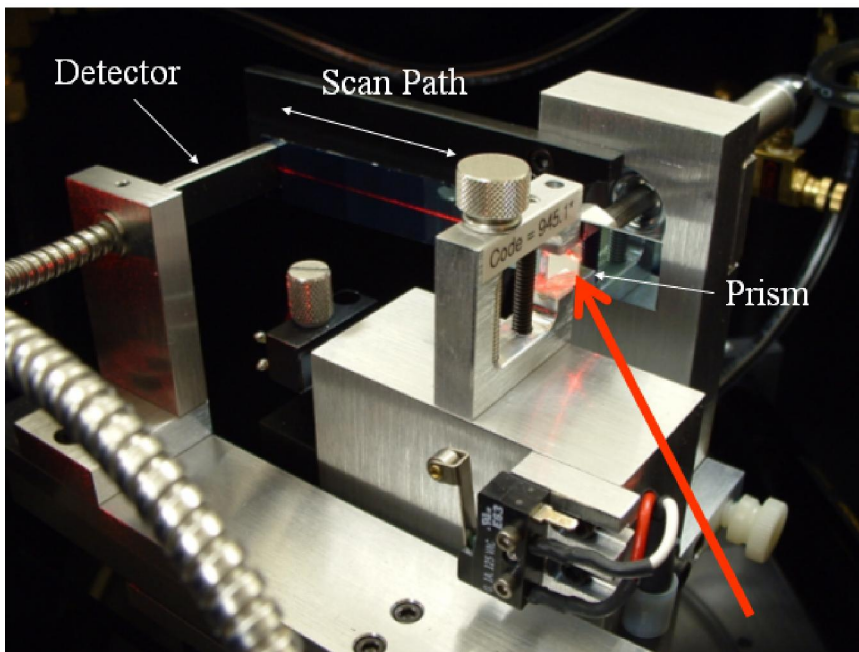


Figure II.4. Photograph of waveguide loss measurement setup.

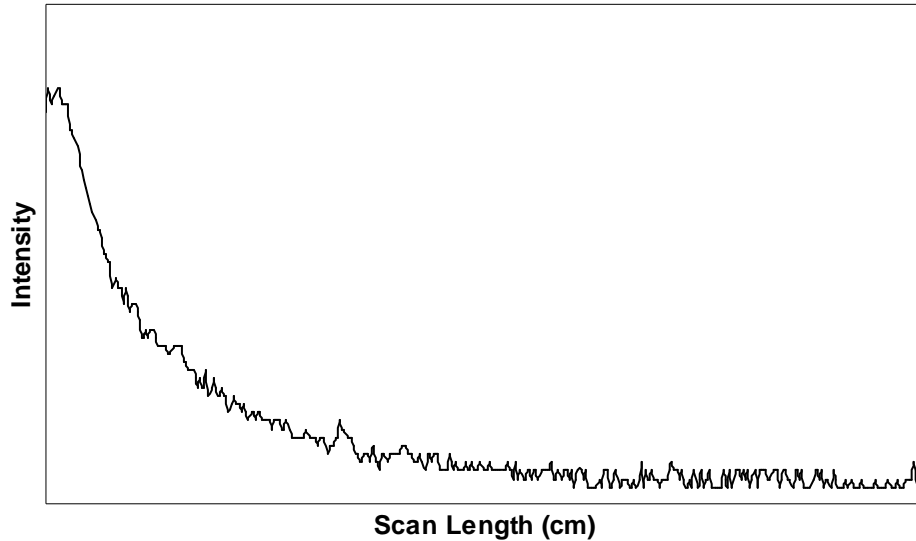


Figure II.5. Exponential curve corresponding to waveguide loss, as measured by a prism coupler.

B. Sol-gel Preparation and Deposition

The barium titanate sol was prepared using the method described by Kozuka et al.⁴⁴ Reagents used were barium acetate (99+% $\text{Ba}(\text{CH}_3\text{COO})_2$; Aldrich), titanium ethoxide ($\text{Ti}(\text{OC}_2\text{H}_5)_4$; Aldrich), polyvinylpyrrolidone ($\text{C}_6\text{H}_9\text{ON}$, MW = 630,000; Alfa Aesar), distilled water (18M Ω), glacial acetic acid (99.9% CH_3COOH ; Fisher) and reagent-grade ethanol (~90% $\text{C}_2\text{H}_5\text{OH}$; Fisher). Components were batched for a 1/1/0.5/5/30/5 mole ratio respectively (the monomer of polyvinylpyrrolidone (PVP) was used in the calculations). Firstly, PVP was dissolved in ethanol and two thirds of the total volume of acetic acid. This process took several minutes of constant stirring. Titanium ethoxide was added drop-wise once the PVP had been completely incorporated. The barium acetate was dissolved in a separate solution of water and the remaining volume of acetic acid. This process step also included several minutes of stirring. The barium

solution was then added drop-wise to the titanium solution and let stir until a transparent sol was achieved. Typical batch size was 100 grams and was of sufficient volume to coat approximately 20 6" wafers.

Thin films of the afore-mentioned sol were deposited onto substrates, which were whole or partial silicon wafers with a thick thermal oxide on top. The silicon wafers were 125mm (5") in diameter with [001] orientation and a single flat. The thermal oxide was a silicon dioxide layer deposited using a flame hydrolysis method. Before coating, each wafer was cleaned with isopropyl alcohol and analyzed using the prism coupler. Cladding thickness and oxide index was measured and logged for future computations. Spin coating was performed using a Model G3-8 Desktop Precision Spin Coating System (Cookson Electronics), shown in Figure II.6. Approximately 2cc of barium titanium alkoxide sol was dispensed onto the wafer using a small syringe equipped with a 0.22 μ m nylon mesh filter. The sol was decanted onto the wafers before they were set into rotation. A spin-up time of 25.5 seconds (the maximum for the coater) was used to allow the sol to spread completely over the surface. The samples were spun coat at speeds from 500 to 2000 rpm for no more than 30 seconds. After spinning was completed, the coated wafer was transferred to a hot plate and dried at 100°C. The wafer was let cool and then cleaved into samples of varying geometries for various heat treatments and testing. Samples were fired in a Lindberg-Blue box furnace. Initially, samples were removed from the furnace at high temperature. It was reported by Kozuka, et al. that samples did not crack, even when being subjected to air quenching from several hundred degrees. However, cracking was observed in the current work. Subsequent samples were let cool to below the transition temperature of BaTiO₃ before removal from the furnace. After

heat treatment, samples were characterized using prism coupling as well as several other physical and microstructure characterization methods.



Figure II.6. Specialty Coating Systems Model G3-8 Desktop Precision Spin Coating System, Cookson Electronics.

C. Thin Film Characterization

Thermal analysis of the sol was performed using an SDT 2960 Simultaneous DSC-TGA (TA Instruments, New Castle, DE). Thermo-Gravimetric Analysis (TGA) and Differential Scanning Calorimetry (DSC) were run simultaneously on the sample. Weight loss of the sol and heat flow of the furnace was monitored as the sample was heated in air from room temperature to 700°C at 10°/min in a platinum tray. Thermal

Advantage software (v 1.1A, TA Instruments) was used to collect data, which was then analyzed using Universal Advantage software (v 3.4C, TA Instruments).

Diffraction experiments were run on a Siemen's Kristalloflex diffractometer using Copper $K\alpha$ x-rays and a Bragg-Brentano Goniometer. Small wafer samples were cleaved and mounted in a side-drift sample holder using X-ray amorphous putty. Data was collected from 10° to $65^\circ 2\theta$ in 0.02° steps, 10 seconds each. Datascan software (v 3.1, Materials Data Inc.) was used to collect intensity data from the diffractometer and Jade software (v 6.0.3, Materials Data Inc.) was used for analysis.

III RESULTS AND DISCUSSION

A. Substrate Characterization

A total of 15 different wafers were used during this study, each having a silica cladding layer with essentially identical intrinsic properties. A typical prism coupling spectrum for the thermal oxide wafers is shown in Figure III.1. The sharp peaks represent the guiding modes for the silica layer. The fundamental mode is represented by a very sharp, deep peak at the highest effective index. In this mode, enough light is being guided that it is plainly visible in a lighted room due to the slight scattering in the silica film. Due to the high thickness of the oxide film and the high index contrast on either side, in excess of 50 modes were detected in this sample allowing for precise calculation of the thickness and index of the thermal oxide. The unique index and thickness of each silica layer was recorded and used in calculations once the barium titanate film was deposited. The thickness of the silica layers varied from wafer to wafer, 18-26 μm , but in each case was thick enough to physically and optically mask the deposited barium titanate thin film from the silicon substrate. The average index of the silica was seen to be 1.457 at 633 nm. The surface of the wafers was highly reflective and homogeneously covered with the oxide.

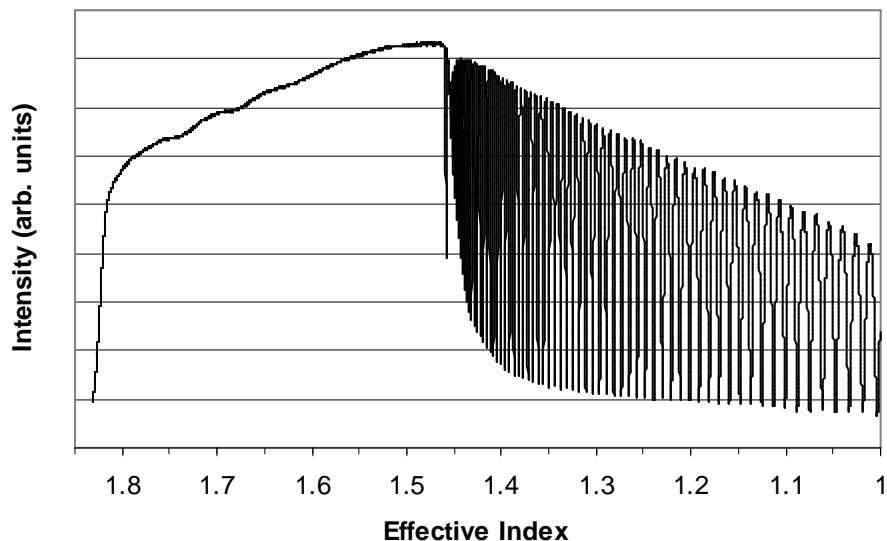


Figure III.1. Prism coupling spectrum of silica thermal oxide on silicon wafer.

B. Sol Preparation and Characterization

Initially, a barium titanium alkoxide sol was prepared using titanium isopropoxide as a metal source and isopropanol as a solvent. This was the original recipe described in the literature by Kozuka et al.⁴⁵ However, the sol lifetime was too short for repeated use of the same stock sol over a reasonable period of time. Inevitably, the batch would gel overnight leaving an opalescent solid mass that was not useable for thin film deposition. Further study of the chemistry of the sol used by Kozuka et al. led to the development of a new recipe capable of forming thin films of the desirable thickness, but with a remarkably longer life.⁴⁴ The Ti metal source in this recipe was titanium ethoxide and the solvent used was ethanol. This sol was prepared using the new procedures and used in all subsequent films as reported in this manuscript.

To understand the specific removal of organics from the film, the sol was subjected to thermal analysis using a combined DSC-TGA. The results of this

experiment are given in Figure III.2. Approximately 80% of the initial mass is lost in heating the sol to 100°C. This loss corresponds to an endothermic peak associated with the evaporation of the solvent at approximately 80°C. The boiling point of ethanol is 78°C but there is no evidence of rapid evaporation of acetic acid at its corresponding boiling point of 118°C. The breadth of the peak suggests the acetic acid is likely evaporating over an extended temperature range, expectedly due to complexation. It is known the titanium ethoxide species undergoes a ligand exchange process in the solution. This would tie up a fraction of the acetate molecules and decrease the total amount of free acetic acid in solution. The free acetic acid can also be expected to be physisorbed on to the metalloxane groups.

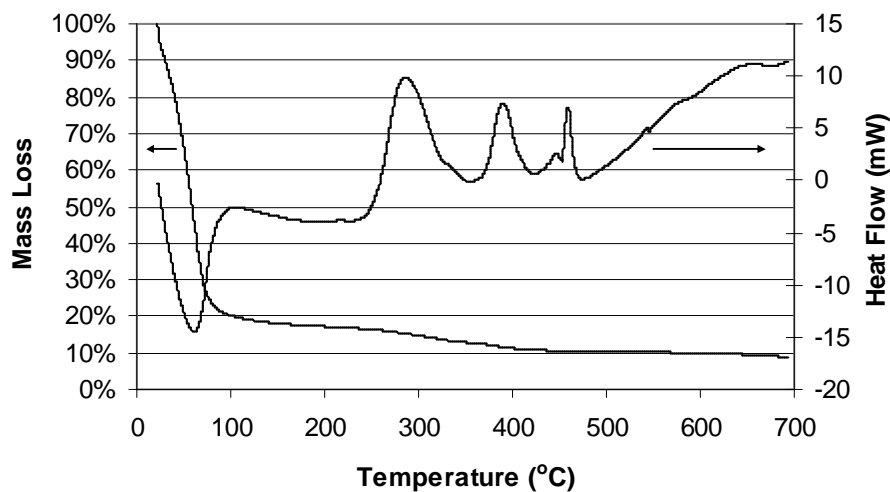


Figure III.2. Simultaneous DSC-TGA of barium titanium alkoxide sol.

The first exothermic peak, occurring at approximately 300°C, corresponds to the combustion of PVP. This mass loss is seen to end at 350°C where next peak begins. This second exothermic peak at 400°C corresponds to the loss of acetate groups from the polymeric structure. The final region of mass loss is complete at 500°C, where the last carbonate species are removed.

C. Effect of Spin Coating Parameters on Film Properties

The first studies conducted were essentially to understand the effects of spin coating parameters on the thickness of the films. The parameters of interest were the spin-up (acceleration) time, spin-off (constant spin speed) time and steady spinning speed. The spin-up and spin-off times had little bearing on the quality of the wafers, provided that the sol completely covered the entire surface early during the ramp. As expected, the spin speed had the most impact on the film thickness. Samples were spun coat at 2000, 1500, 1000 and 500 rpm then dried on a hot plate at 100°C. These gel films were analyzed using prism coupling, as deposited. The results of these tests are shown in Figures III.3-6.

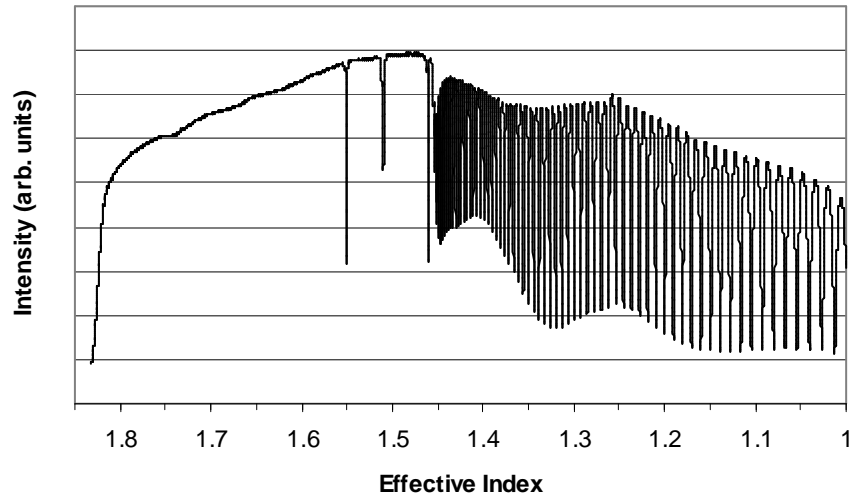


Figure III.3. Prism coupling spectrum of gel film spun coat at 2000 rpm.

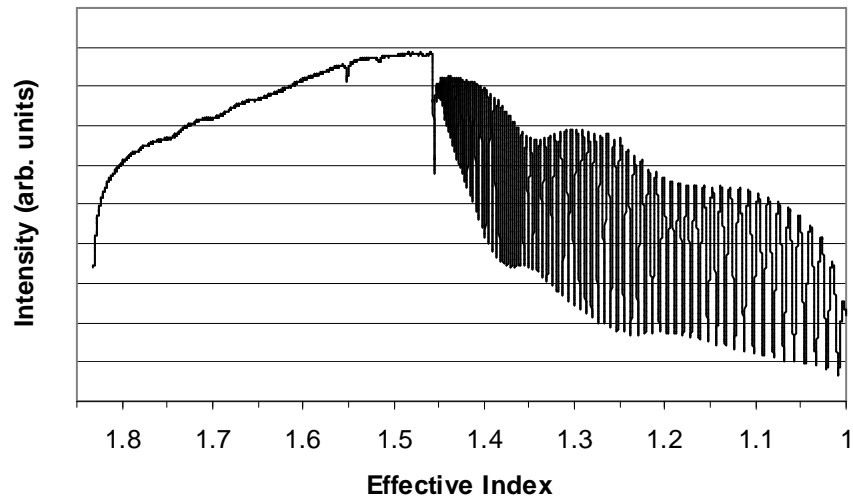


Figure III.4. Prism coupling spectrum of gel film spun coat at 1500 rpm.

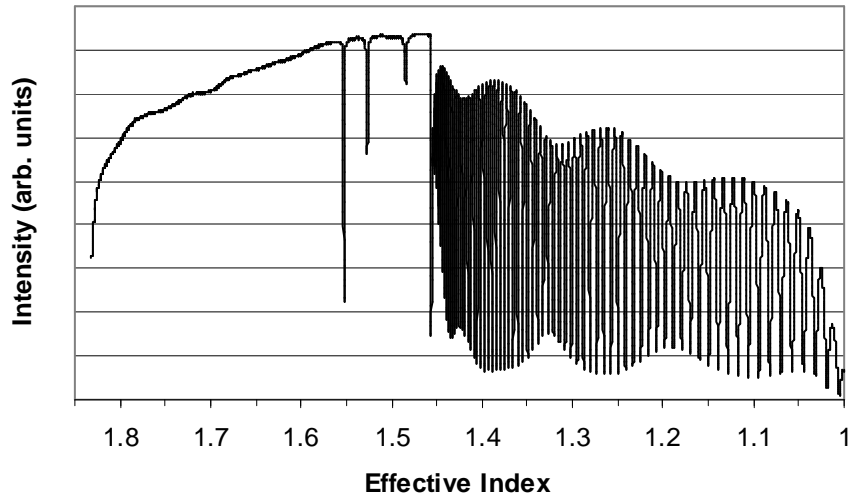


Figure III.5. Prism coupling spectrum of gel film spun coat at 1000 rpm.

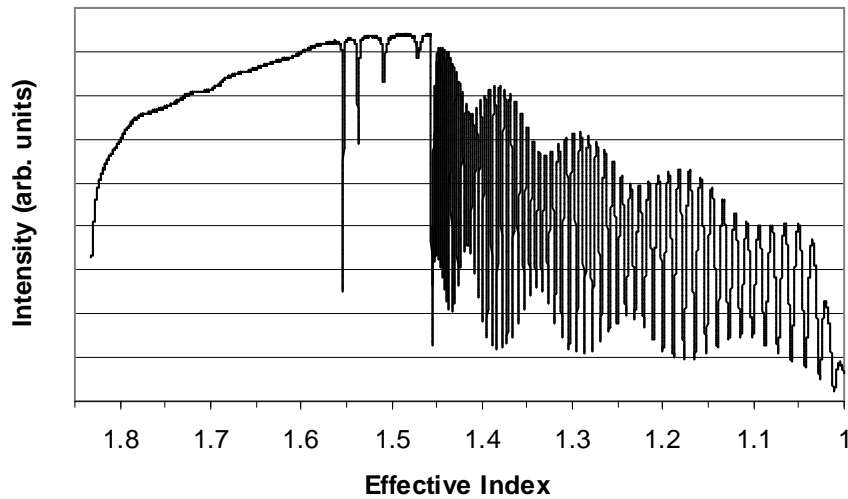


Figure III.6. Prism coupling spectrum of gel film spun coat at 500 rpm.

According to these measurements, the index of the gel films is 1.56 ± 0.01 . As seen in Figures III.3-6 and in Table III, the effective index of the first mode, TE_0 , is relatively unchanging. However, the peaks corresponding to the higher-order modes shift

to higher effective index with decreasing speed. The thickness of the films is also given in Table III and is represented graphically in Figure III.7. The response of gel thickness to spinning speed appears to be linear in the region tested. A linear curve fit was applied to the data with acceptable statistical significance.

Table III. Prism Coupling Data Collected from Gel Films

Spin Speed (rpm)	Effective Mode Index				Film Index		Film Thickness	
	TE ₀	TE ₁	TE ₂	TE ₃	n	Δn	t (μm)	Δt(μm)
2000	1.5506	1.5099	--	--	1.5644	--	1.2583	--
1500	1.5514	1.5158	1.4637	--	1.5632	0.0002	1.3799	0.0106
1000	1.5527	1.5268	1.4844	--	1.5614	0.0000	1.6484	0.0044
500	1.5536	1.5370	1.5090	1.4714	1.5592	0.0000	2.1240	0.0089

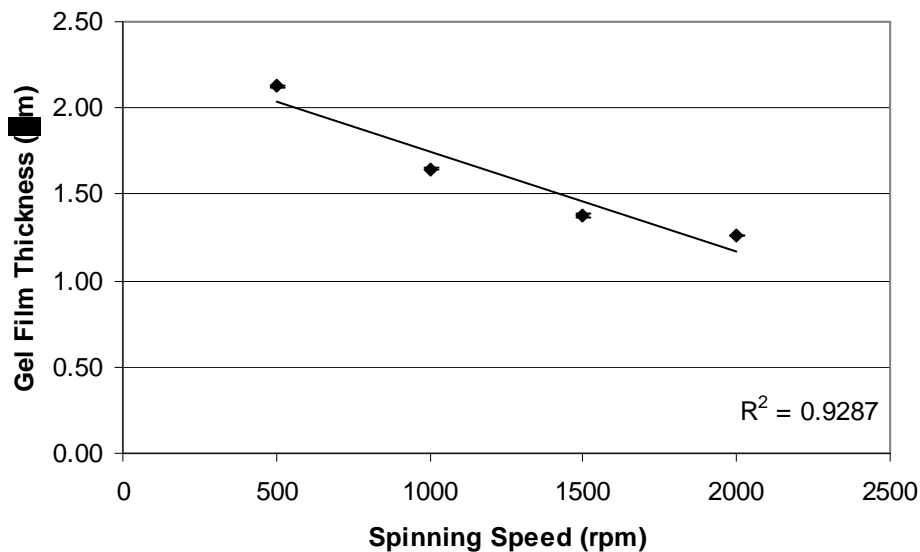


Figure III.7. Thickness of gel films as a function of spinning speed. (Note: Error bars obscured by marker.)

In addition to the trend in thickness, several other important observations can be made. The first deals with peak shape: they are relatively narrow. This is evidence of ideal coupling and low coupling loss of the guided modes. Additionally, the peak corresponding to the fundamental silica mode, appearing at effective index of 1.46, is narrow and sharp, indicating low loss coupling to the reflection mode. With the primary desired goal of this work being the production of a low-loss waveguide, this data suggests that the initial film meets the needs and provides a desirable starting point.

The second observation here is the multimodal behavior of the gel films. The thinnest film, at 1.25 micrometers, is capable of sustaining two modes while the thickest, at roughly 2 micrometers, is capable of supporting four modes. However it must be noted that, from first principles, the higher order modes are excited with insignificant power. This is key to being able to use thicker films that allow for relative ease of coupling as Quasi Single Mode waveguides.

The third observation is evidenced in the difference in modal coupling quality seen in the 1500 rpm sample. This sample highlights the possibility of generating artifacts during the prism coupling measurement. We must bear in mind that the gel film is physically being pressed against the face of a hard prism. At this point in the processing, the gel film is still unfired and susceptible to scratches and other external defects. The act of pressing the film against the prism puts a significant amount of pressure on the gel and is evidently capable of distorting it at the coupling spot. This observation places emphasis on the importance of making good contact initially, or else it can be virtually impossible to measure the spectrum effectively without irreversibly damaging the surface of the sample.

D. Effect of Heating Rate on Film Properties

The thermal cycle described earlier by Kozuka, et al. involves heating the samples in several different steps. The first step is heating to 300°C for 10 minutes, during which the solvent is driven from the gel. The thermal analysis conducted earlier would also suggest some organic is combusted at this temperature. The second step is to heat at 500°C for 10 minutes, where the entire organic content of the film is removed. Final heat treatment is at 700°C for 10 minutes, which crystallizes the film. No mention is made of the heating rates in any of the articles. Heating rate is an important consideration as it has ties to the kinetics of crystal nucleation and growth as well as in/out diffusion of gases through the film.

A series of four samples were prepared for this study by spin coating at 1000 rpm. The first sample was heated at a constant rate of 5K/minute for the entire cycle. The second was heated at 10K/minute. The third sample was given a longer time to drive off organics. It was heated at 5K/minute from room temperature to 300°C and from 500°C to 700°C, but only 0.5K/minute from 300°C to 500°C. The final sample was heated stepwise to each temperature level. Due to the relatively large volume of cavity of the box furnace used (~1 cfs), 30 minutes of dwell time at each temperature was used to fully equilibrate the sample. The thermal cycles used for these samples are shown schematically in Figure III.8. For all practical purposes, a 5 minute ramp time was assumed for the fourth sample (or approximately 40K/minute).

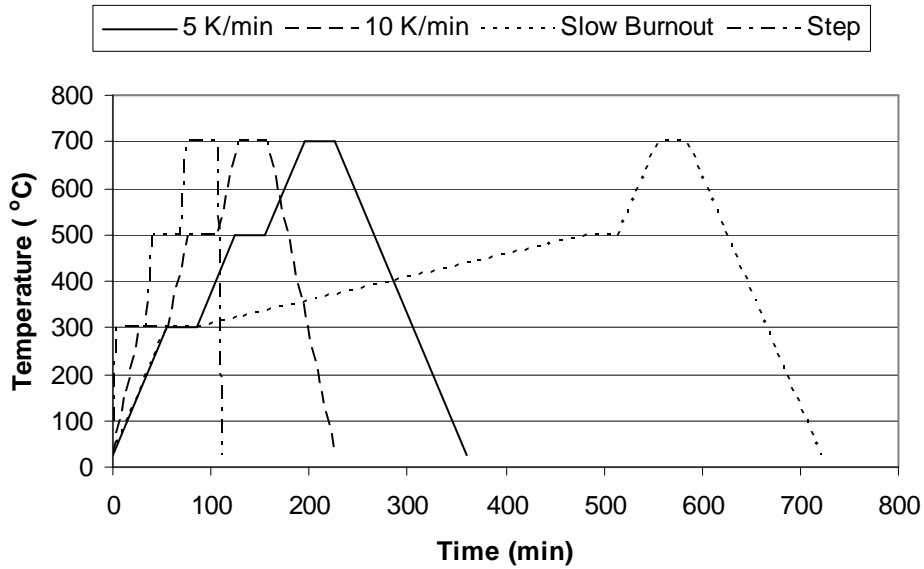


Figure III.8. Thermal cycles for Samples 1-4, showing different heating rates.

Once these samples had cooled, they were analyzed using the prism coupler. The results of these tests are given in Figures III.9-12. Firstly, the sharp, narrow peaks seen in the as-coated gel films (for example, Figure III.5) were replaced by broad, diffuse ones. This indicates a high coupling loss in the films, presumably due to greater surface scattering. Visual inspection of the films corroborates this result as the films appear to be opalescent. The first three samples, those heated at slower rates, were all lossy, showing a hazy blue surface. The fourth sample, which was stepped to temperature, showed somewhat less scattering. There appears to be a marbled texture of areas that scatter less light than others.

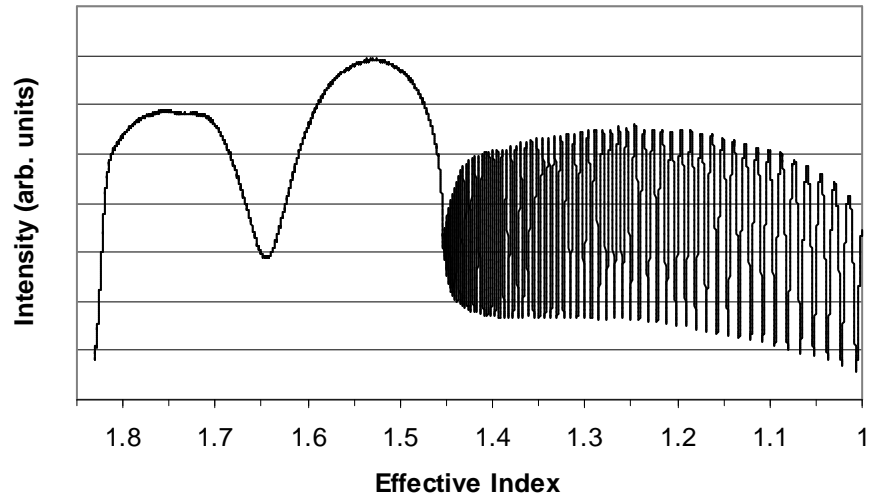


Figure III.9. Prism coupling spectrum of sample heated at 5K/minute.

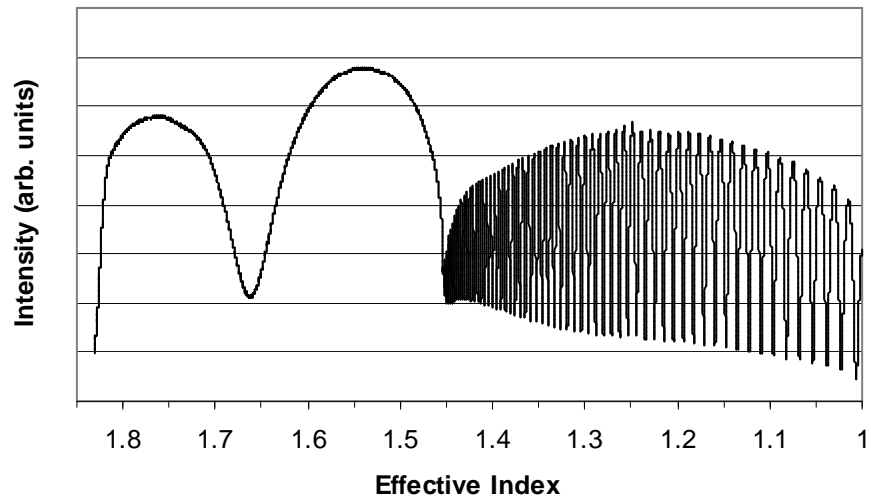


Figure III.10. Prism coupling spectrum of sample heated at 10K/minute.

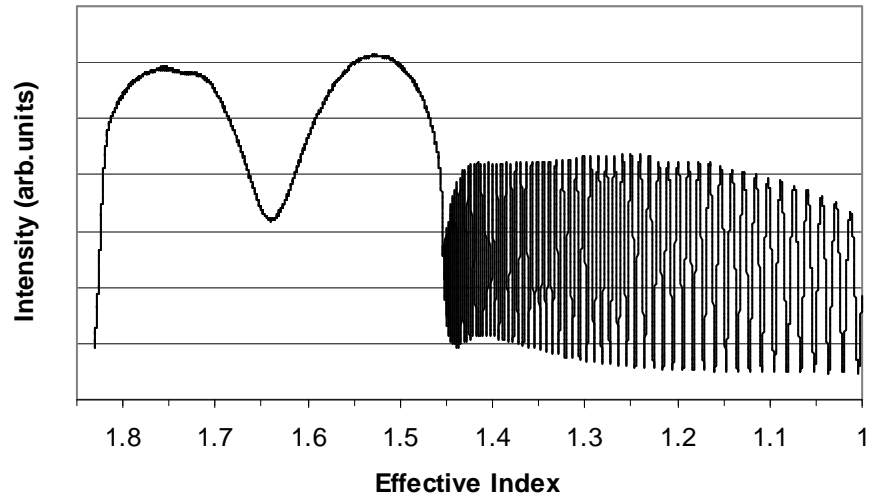


Figure III.11. Prism coupling spectrum of sample heated at 0.5K/minute from 300°C to 500°C.

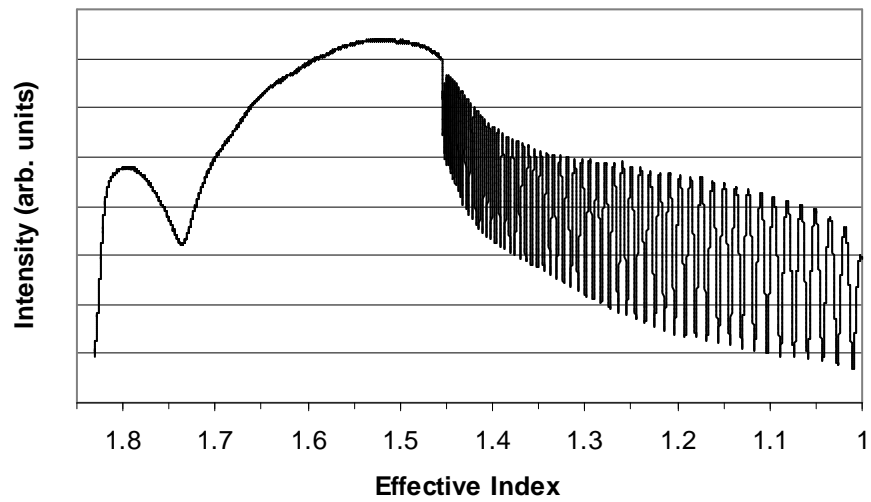


Figure III.12. Prism coupling spectrum of sample step heated to temperature.

The second observation is the fact that only one guiding mode peak was detected. Note that others may in fact exist, but they are either below the cladding mode cut-off or they are indiscernible due to peak broadening. This inhibits the extraction of the film index and thickness from this data; however the fundamental mode can still reveal qualitative data about the films.

Firstly, the peak shape is different for the stepped sample (Figure III.12). The peak is shallower and less broad than the others, suggesting lower loss. Since the shape of the peak can be altered by changing the manner of coupling light, it should be noted that the same coupling pressure was used for each sample and the angle of incidence of the laser to the prism was not altered in any way that would change the coupling strength. Secondly, the mean position of the mode, although not an absolute match to the film index, is still an indicator of the magnitude of the film index. In this case, it is clear that the index of the fourth film exceeds that of the other three samples. An approximation of this effect can be modeled as shown in Figure III.13, by plotting the amount of time the sample is held at elevated temperature against the effective index of the fundamental mode, TE_0 .

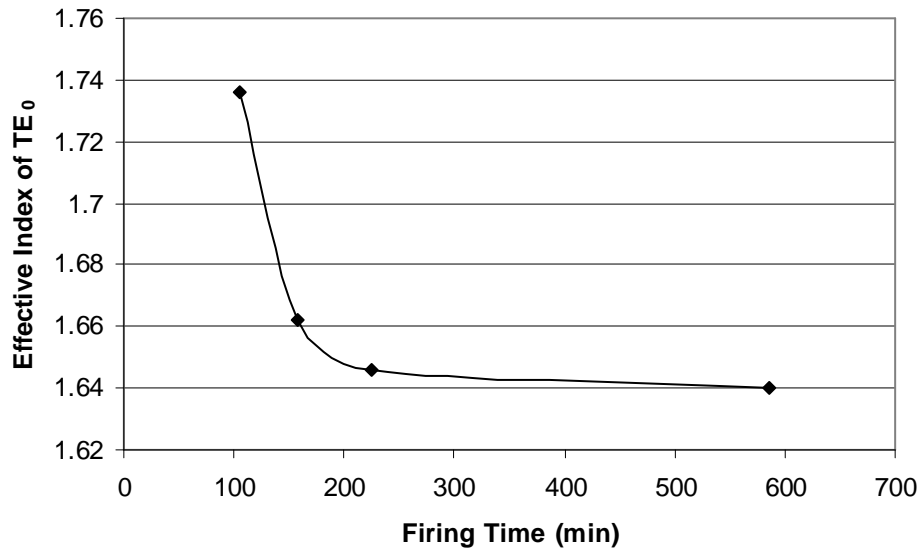


Figure III.13. Effective index of TE₀ as a function of firing time.

These four samples were further characterized in X-ray diffraction experiments. The results of these tests are shown in Figures III.14-17. The diffraction pattern for each sample indicates the formation perovskite barium titanate as desired. Some details are worth mentioning. The additional amorphous band seen approximately centered at 22° 2θ is due to the silica cladding. The figures also show the peaks corresponding to the silicon substrate, one at 62° 2θ for the [400] $K\beta$ reflection and in the case of Figure III.14 another at 33° 2θ for the [200] reflection. The 5K/min sample exhibits some peak splitting, indicating incomplete crystallization. The noise at higher angles suggests the 10K/min sample is crystallized even less. From this data we conclude that only the 0.5K/min and stepped samples are fully crystallized.

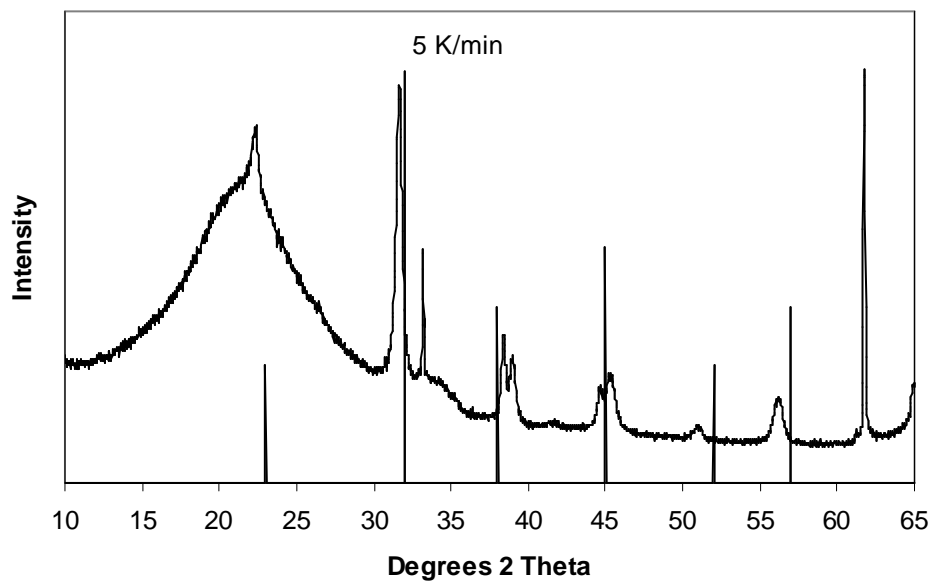


Figure III.14. X-ray diffraction pattern of sample heated at 5K/minute; crystallite size, 196Å. (BaTiO₃ peak lines included)

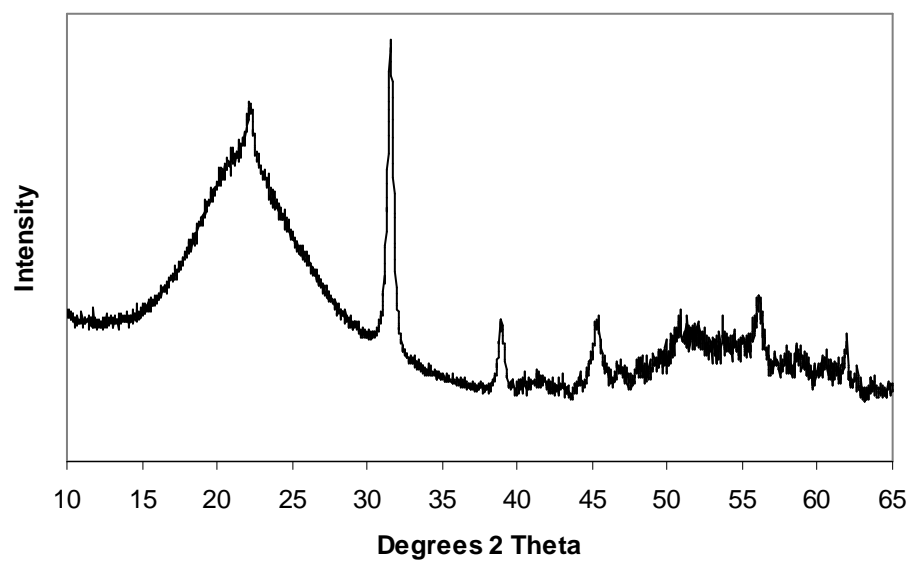


Figure III.15. X-ray diffraction pattern of sample heated at 10K/minute; crystallite size, 181Å.

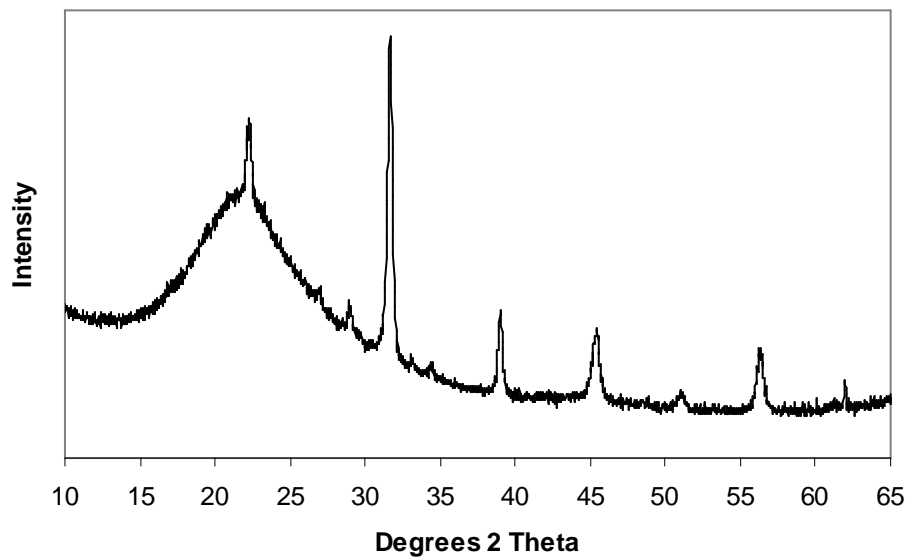


Figure III.16. X-ray diffraction pattern of sample heated at 0.5K/minute from 300°C to 500°C; crystallite size, 260Å.

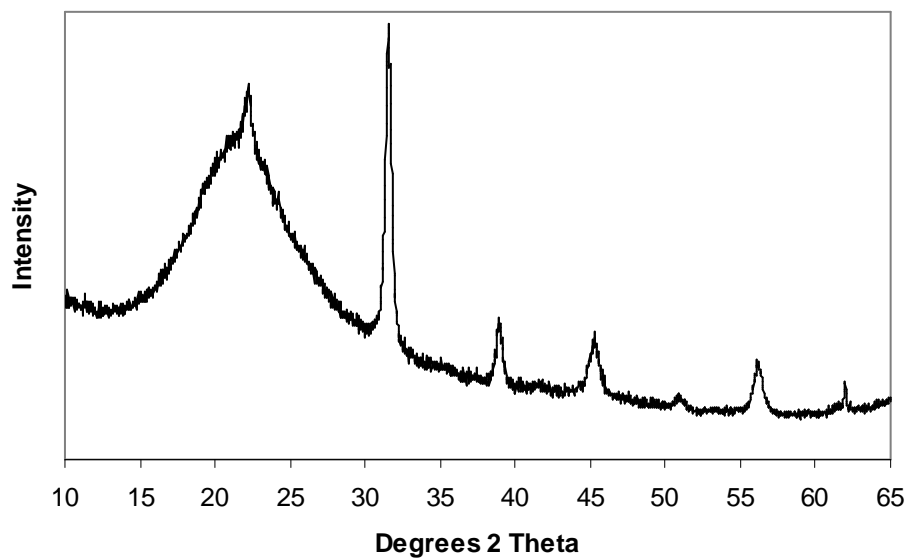


Figure III.17. X-ray diffraction pattern of sample step heated to temperature; crystallite size, 173Å.

The diffraction pattern of the sample heated slowest (0.5K/min) shows some peaks at low angles, in particular one at 29° (2θ), which cannot initially be accounted for. This particular peak is located in the middle of two pyrochlore phases: Ba₂TiO₄ at 29.3° and BaTi₃O₇ at 28.4°. The Cu K_β line for stoichiometric barium titanate is also located at 28.4° 2θ. Back-calculation of the sol batch reveals a 1.00065:1 cation ratio, barely in favor of the excess barium phase to account for the Ba₂TiO₄ pyrochlore. However, reaction kinetics stipulate temperatures in excess of 1100°C for the formation of this phase.⁴⁸ The presence of two smaller peaks flanking the 29° peak, Tungsten L lines, suggest the spurious peak is in fact the Cu K_β peak. Based on this data, the only crystalline phase detectable is a BaTiO₃ perovskite.

The Scherrer equation⁴⁹ was used to calculate crystal sizes using the [110] peak:

$$\tau = \frac{K\lambda}{\beta_{\tau} \cos\theta} \quad (16)$$

where β_τ is the breadth of the peak, θ is the sample angle and K is a shape factor, usually taking the value of 0.9. Figure III.18 shows the crystal sizes plotted against time at elevated temperature, similar to the prism coupling figure. There is a good correlation of this data to a linear curve fit indicating small grains result from a faster heating cycle. The crystals are nanosized in each case, which is desirable for reduced scattering of light. From this viewpoint, the high loss in the film is somewhat mysterious and requires more analysis, which is presented later.

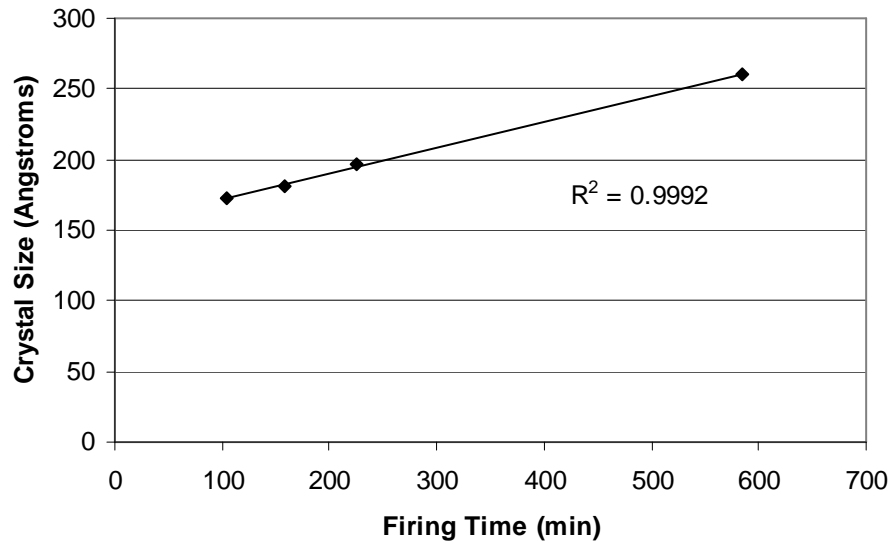
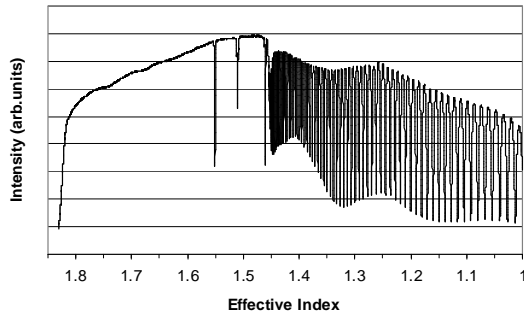


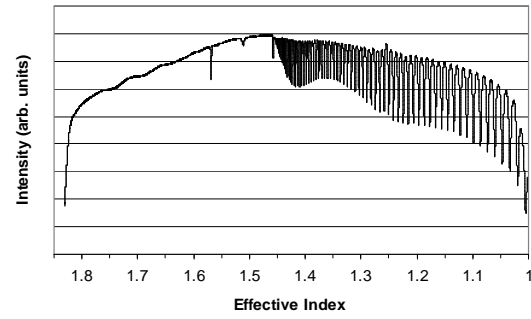
Figure III.18. Crystal size as a function of time at elevated temperature.

E. Effect of Insertion Temperature on Film Properties

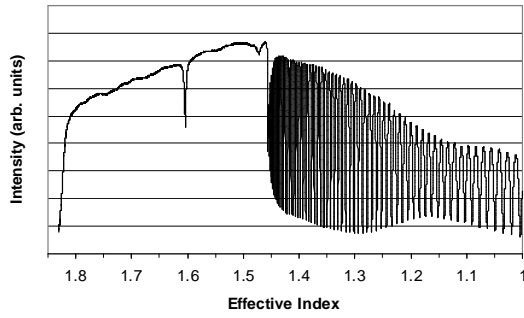
The experiments described hitherto suggest that samples directly inserted into the heated furnace (rapid thermal anneal) produce films with smaller crystal size, a higher index and lower loss. Therefore, seven samples were prepared from each of the four wafers used in the first experiment. Each sample was heat treated at a different temperature in 100K increments, from 100°C up to 700°C. After cooling, samples were visually inspected for cracking or other defects and then tested using the prism coupler. The results of these tests are given in Figures III.19-22.



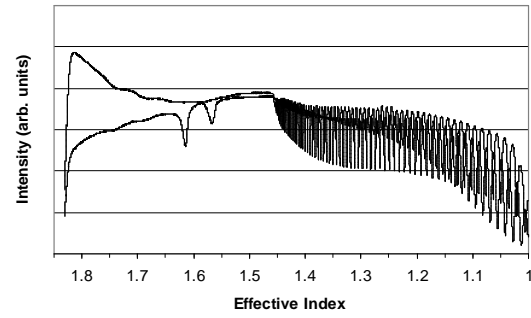
a) Sample inserted at 100°C



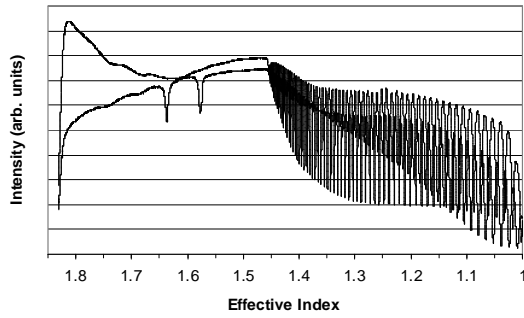
b) Sample inserted at 200°C



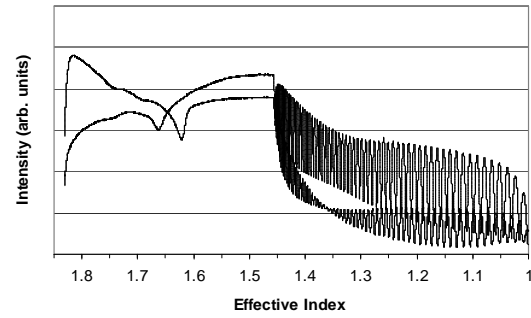
c) Sample inserted at 300°C



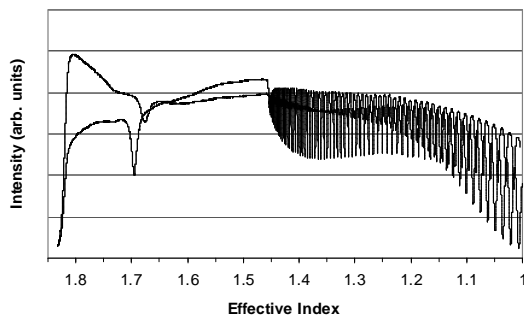
d) Sample inserted at 400°C, TE/TM



e) Sample inserted at 500°C, TE/TM

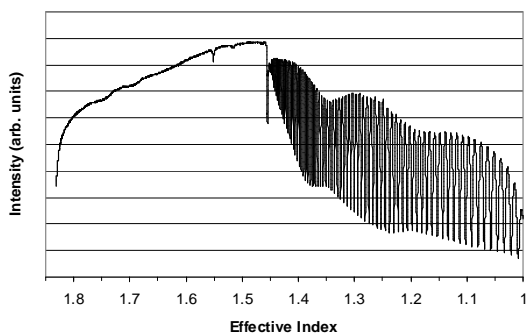


f) Sample inserted at 600°C, TE/TM

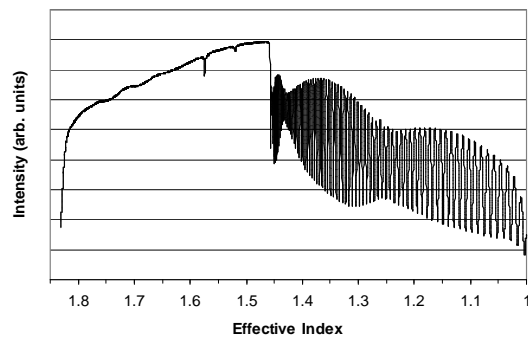


g) Sample inserted at 700°C, TE/TM

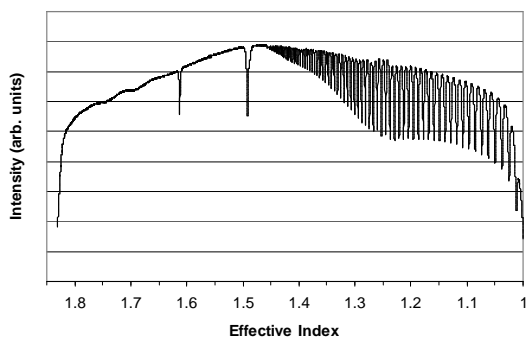
Figure III.19. Prism coupling spectra of samples spun cast at 2000rpm.



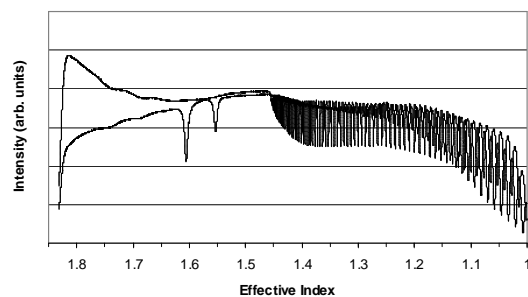
a) Sample inserted at 100°C



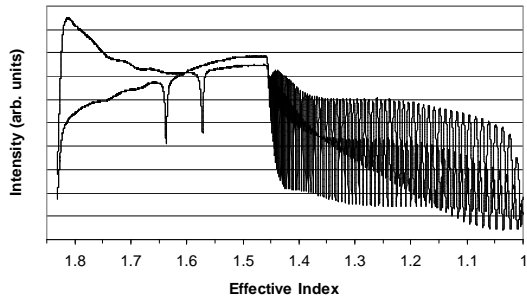
b) Sample inserted at 200°C



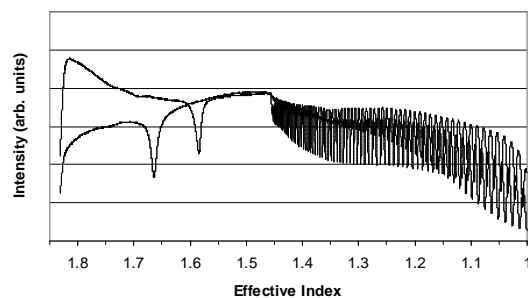
c) Sample inserted at 300°C



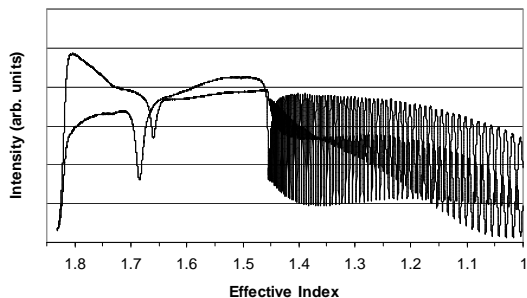
d) Sample inserted at 400°C, TE/TM



e) Sample inserted at 500°C, TE/TM

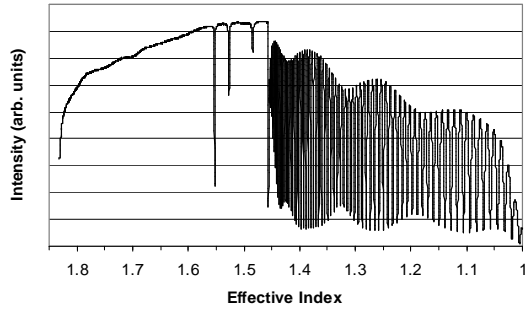


f) Sample inserted at 600°C, TE/TM

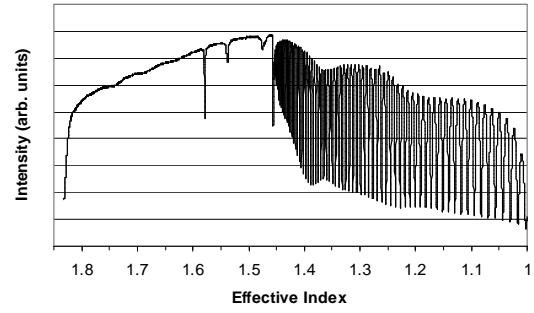


g) Sample inserted at 700°C, TE/TM

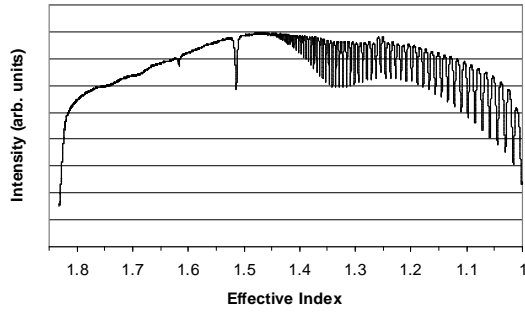
Figure III.20. Prism coupling spectra of samples spun cast at 1500rpm.



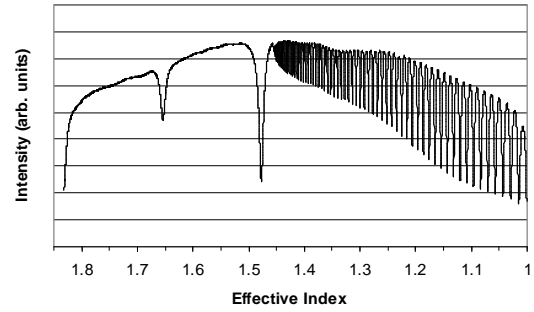
a) Sample inserted at 100°C



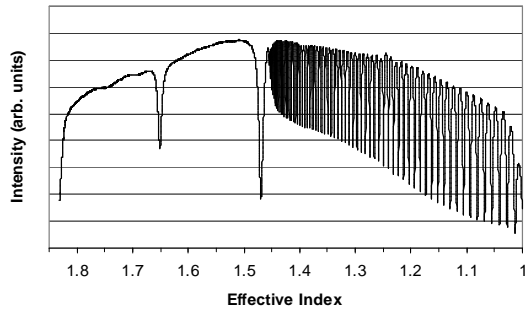
b) Sample inserted at 200°C



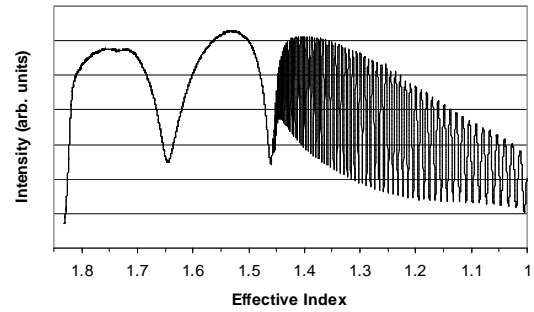
c) Sample inserted at 300°C



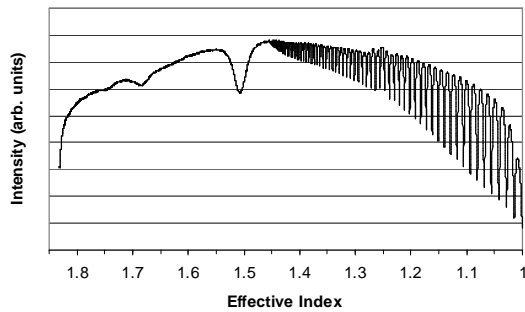
d) Sample inserted at 400°C



e) Sample inserted at 500°C

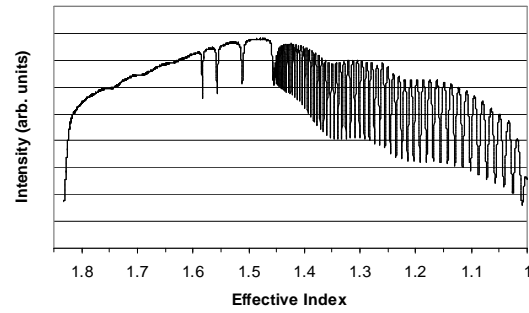
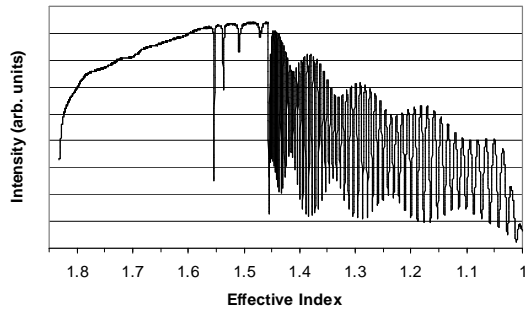


f) Sample inserted at 600°C



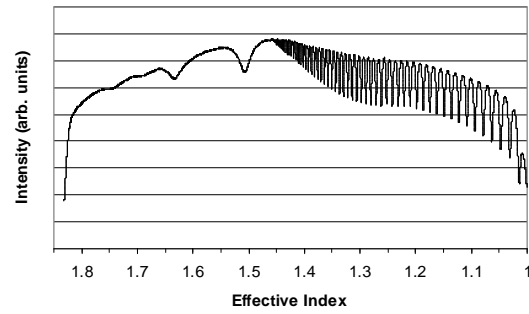
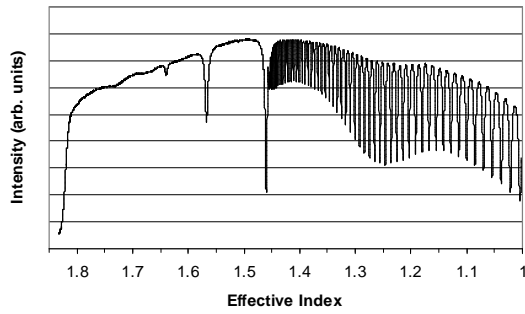
g) Sample inserted at 700°C

Figure III.21. Prism coupling spectra of samples spun cast at 1000rpm.



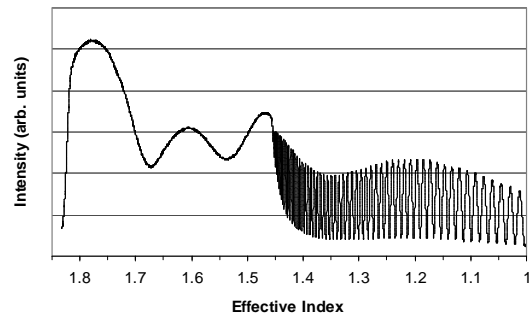
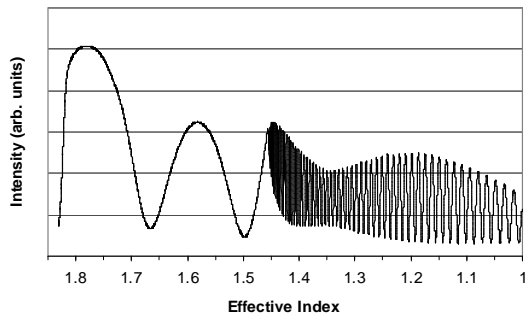
a) Sample inserted at 100°C

b) Sample inserted at 200°C



c) Sample inserted at 300°C

d) Sample inserted at 500°C



e) Sample inserted at 600°C

f) Sample inserted at 700°C

Figure III.22. Prism coupling spectra of samples spun cast at 500rpm.

Several important things are worth discussing here. The first is that the thickest film heated to high temperatures, (that is, the sample spun at 500 rpm) displays the same broad peaks that were noted in previous experiments. These broad peaks suggest lossy behavior that is also visually validated by the hazy blue color now obvious to the observer. There appears to be a broadening of the peaks beginning at 400°C, right after the expected removal of the large polymer PVP. This peak broadening is accompanied by a sharp increase in loss, presumably due either to scattering or absorption. We would typically ignore absorption as a loss mechanism, but at 400°C burnout of organic materials is still on-going. Bearing in mind that 400°C is an insertion temperature, the high speed at which the film reaches this temperature adds the possibility of partially charring the sample and leaving behind carbonaceous residue. This scenario is likely in the case of the thickest film, 500rpm, where the 400°C sample was brownish in hue. This implies that thicker films cannot be heated faster, nor perhaps as fast, as thinner ones.

Cracking was also a problem for many of these films. With the exception of the samples spun cast at 2000 rpm, every sample cracked upon cooling. Even at the lowest temperatures used, the heat treatment exceeded the Curie temperature of barium titanate. Stresses incurred in the film upon cooling and due to the transition resulted in macroscopic cracks in most of the films. These cracks also complicated the prism coupling measurement, decreasing the coupling strength. For these reasons, much of the further analyses were conducted on the thinner films only.

The noticeable trend for films heated to lower temperatures is the decreasing effective index of the higher order modes. This is a direct result of the film decreasing in thickness. At the higher temperatures, there is also a trend of the fundamental mode

moving towards higher indices. This is a result of the film index increasing due to densification and eventually crystallization. The calculation of these two parameters, shown in Figures III.23-24, provides us with a clearer picture of the effects of heat treatment. At lower temperatures, the film loses mass due to organic burn-off. This leads to a collapse of the porous matrix due to high capillary stress and consequently a decrease in the thickness of the film and a small increase in the refractive index. At higher temperatures, there is little organic material left and thickness continues to decrease as sintering and crystallization take place. This is accompanied by a continued increase in the index of the material. Additionally, the two parameters are plotted against each other in Figure III.25.

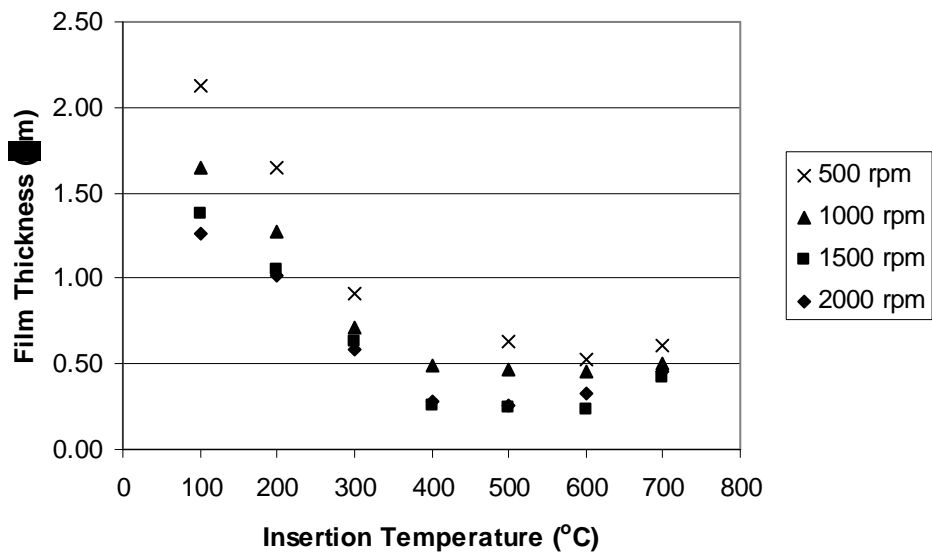


Figure III.23. Film thickness as a function of insertion temperature.

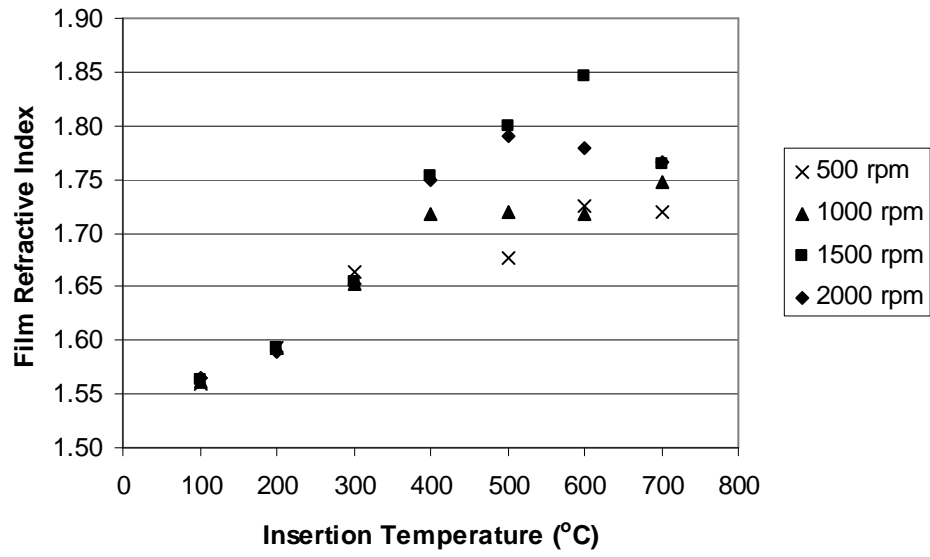


Figure III.24. Film refractive index as a function of insertion temperature.

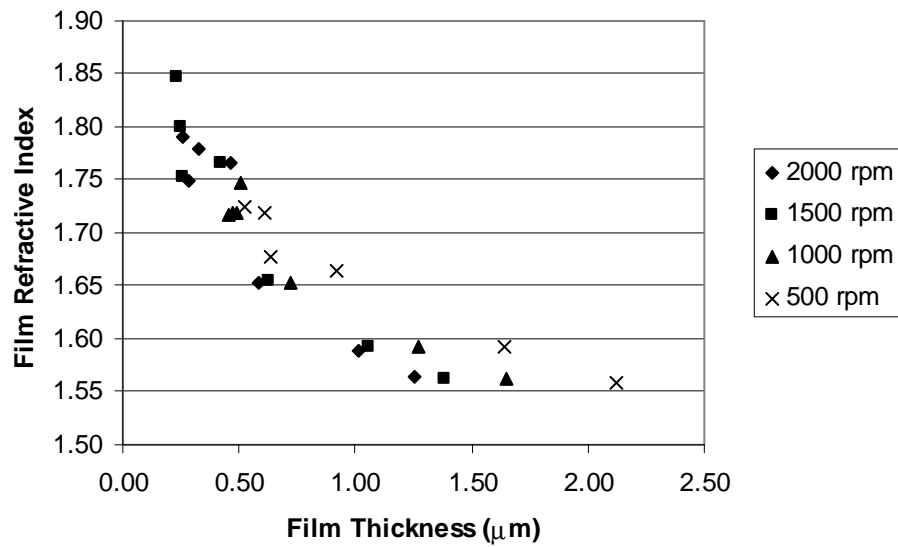


Figure III.25. Film refractive index as a function of film thickness.

Drying the film on the hot plate after spin coating results in the evaporation of the ethanol solvent. Heat treatment to 200°C drives off residual acetic acid, and the onset of 300°C begins the decomposition of PVP with the associated decrease in thickness. Burn-off of PVP is still apparently incomplete at this time according to thermal analysis, but completed at 400°C in addition to the onset of acetate removal. At this point, the heating rate to 400°C begins to exceed the diffusion rate for the organics out of the porosity in the film. In one of the thicker films, charring occurs. Heat treatment to 500°C and higher completes burn-off of organics, albeit at a faster rate than before, and continues to increase the index of refraction. At 700°C, the index of refraction is suspiciously low, about 1.75. The bulk index of barium titanate is approximately 2.46, but after heating to temperatures reported to crystallize the film, the index is very low.

The crystallinity of the films at this point in their processing was characterized by X-ray diffraction. The two films of most interest were those spun coat at 2000 rpm and heated to 500°C and 700°C. It is these temperatures that films are heated to in the thermal cycle designed by Kozuka, mentioned earlier. The results of these two tests are given in Figures III.26-27.

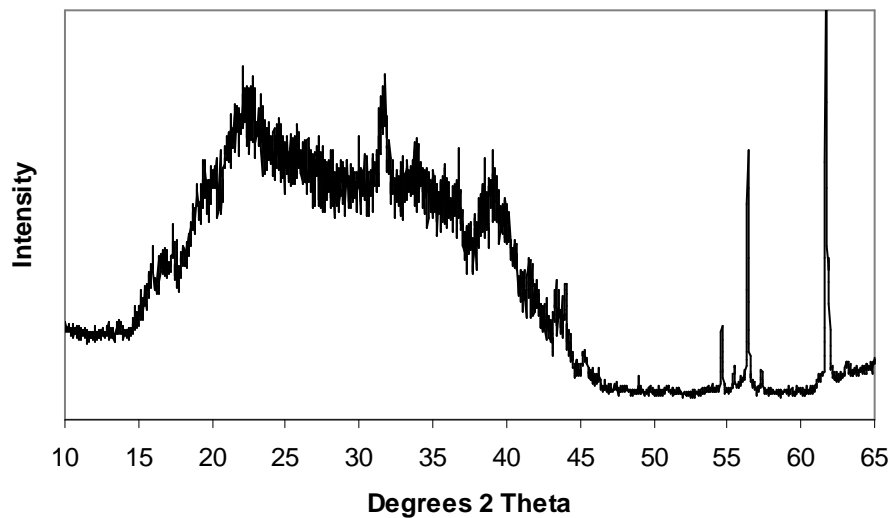


Figure III.26. X-ray diffraction pattern of sample spun coat at 2000 rpm and heated to 500°C.

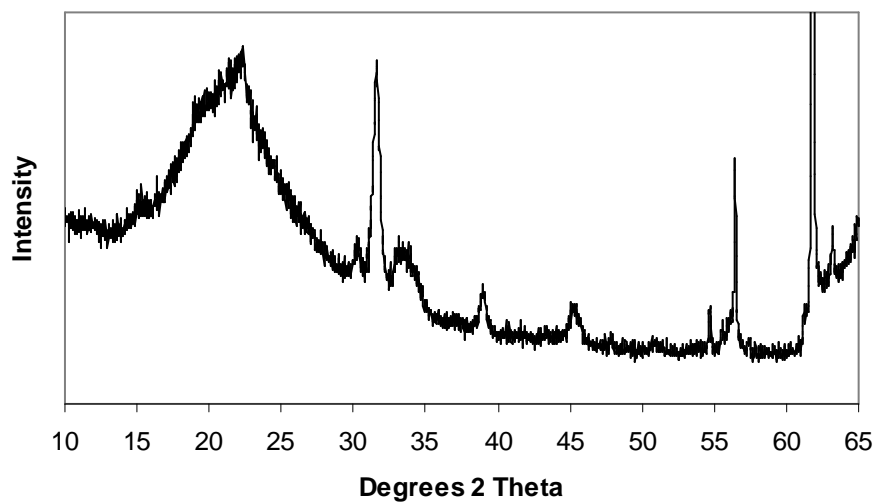


Figure III.27. X-ray diffraction pattern of sample spun coat at 2000 rpm and heated to 700°C.

It appears that at 500°C the sample has only begun to crystallize. The [110] major peak is just beginning to distinguish itself from the amorphous region at $32^\circ 2\theta$. The substrate peaks, at higher angles, are still plainly visible indicating very little X-ray attenuation by the amorphous film. At 700°C, the film is still crystallizing, but is yet to complete the process. The substrate peaks are still visible and all of the perovskite peaks are not yet distinguishable.

Two more samples were prepared to better understand this phenomenon. The first was inserted into a furnace at 500°C and then at 700°C, each time for 30 minutes. The second was inserted at 300°, 500° and 700°C as the very first test was conducted. After they had cooled, they were analyzed using the prism coupler and used in an X-ray diffraction experiment. The results of these tests are shown in Figures III.28-31. The crystallite size and optical information is summarized in Table IV. The substrate peaks are still visible in the XRD pattern for the latter sample, indicating poorer X-ray attenuation by the yet thicker film. The refractive index of the 500°, 700°C sample is higher and the diffraction pattern lacks substrate peaks. These data indicate that consecutive heat treatment at 500° and 700°C fully crystallizes the film better than treatment at 300°, 500° and 700°C.

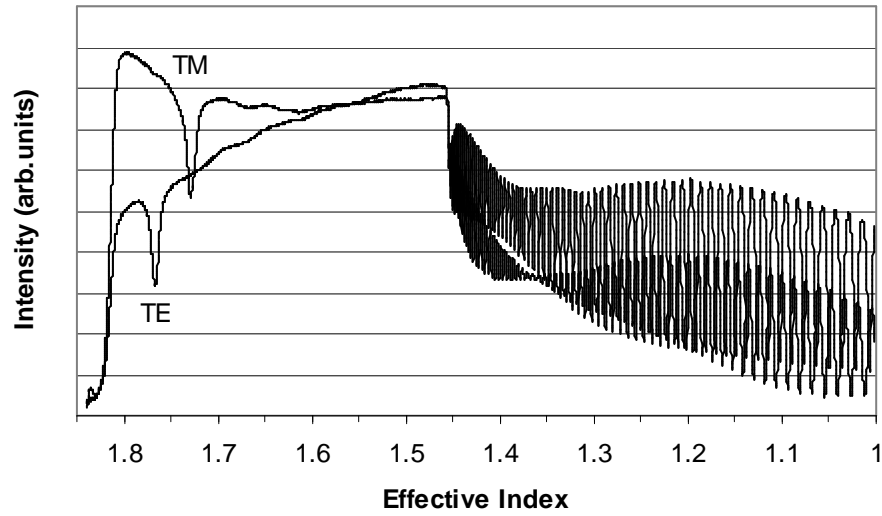


Figure III.28. Prism coupling spectrum of sample spun coat at 2000 rpm and heated to 500°C then 700°C, TE/TM.

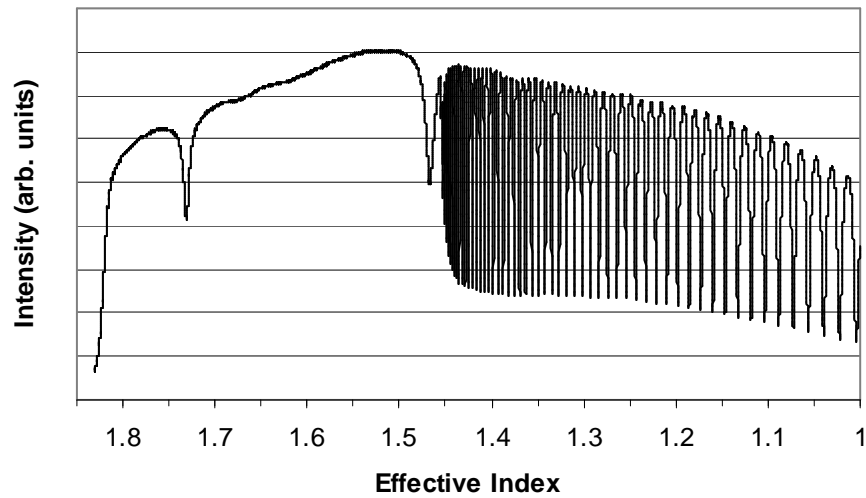


Figure III.29. Prism coupling spectrum of sample spun coat at 2000 rpm and heated to 300°C, 500°C and 700°C.

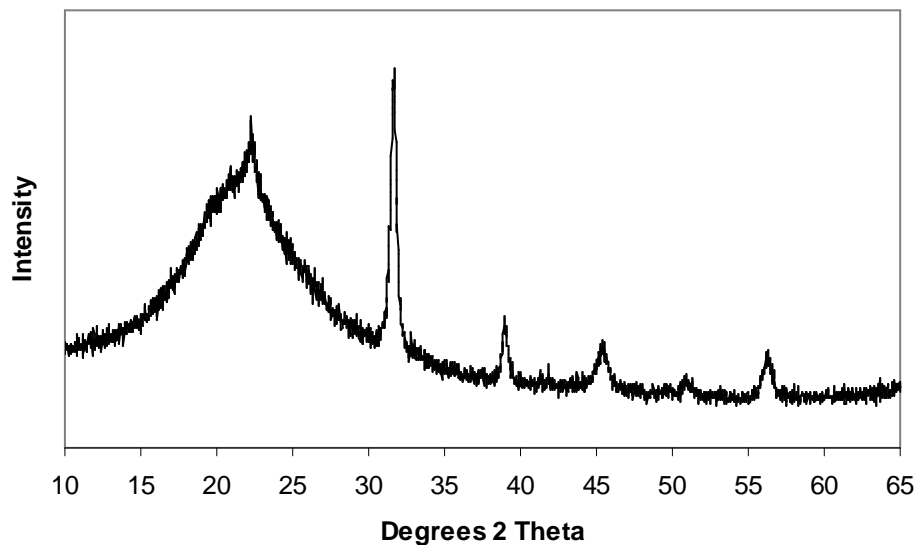


Figure III.30. X-ray diffraction pattern of sample spun coat at 2000 rpm and heated to 500°C then 700°C.

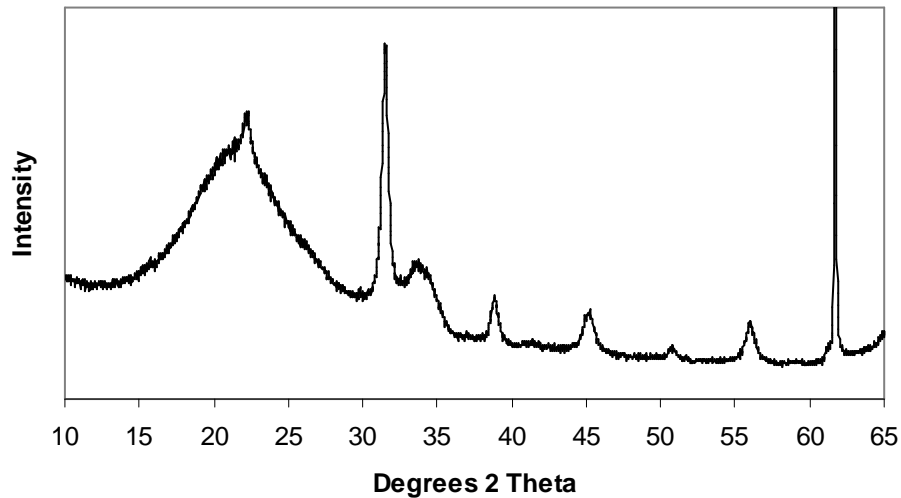


Figure III.31. X-ray diffraction pattern of sample spun coat at 2000 rpm and heated to 300°C, 500°C and 700°C.

Table IV. Optical Properties and Crystallite Size of Fired Films

Heating Profile	Effective Mode Index			Film Index	Thickness	Crystal Size
	TE ₀	TE ₁	TM ₀	n	t (μm)	(Å)
500	1.6369	--	1.5771	1.7906	0.2572	156(14)
700	1.6957	--	1.6752	1.7669	0.4603	180(10)
500,700	1.7666	--	1.7292	1.8674	0.3664	199(5)
300,500,700	1.7310	1.4672	--	1.8271	0.3772	178(6)

The refractive index of the fired films is still low in comparison to the value typically assigned to the bulk, 2.46. Thin films tend to have lower indices than those seen in the bulk. But an index of ~1.87 in the fully crystallized ceramic may be an indication of a significant volume fraction of porosity. This is surprising given that pore channels in the sol are very fine, of nanometer scale. The removal of PVP from the matrix may also contribute to this problem. The incorporation of the polymer into the gel film may facilitate disjointed solid domains upon its combustion that require larger time-temperature products during sintering.

F. Effect of Insertion Temperature on Waveguide Loss

The optical loss in the fired samples was so high that there was no visible trace of the laser through the film. This implies significant attenuation within the first few millimeters of travel. This is in sharp contrast to the bright, continuous ray traces observed during the experiments with the unfired gel. Loss measurements on these as-coated films yielded loss values of approximately 1 dB/cm. This is a desirable loss value. But the loss in the fired samples was immeasurable using the prism coupler, whose detection range truncates at 30 dB/cm. No data has been collected on the loss of the films heated to intermediate temperatures.

For studying the mechanisms for loss, a wafer was prepared by spin coating at 2000 rpm. The film was dried on a hot plate and several pieces of the coated wafer were cleaved for into long samples. These samples were inserted into a hot furnace at several temperatures and the waveguide loss was measured at the fundamental mode. The results of these tests are shown in Figures III.32-35. The non-exponential peaks in these patterns are the result of extrinsic defects in the film, such as scratches in the surface. Yet it is possible to derive meaningful loss values as long as the loss is reasonably low.

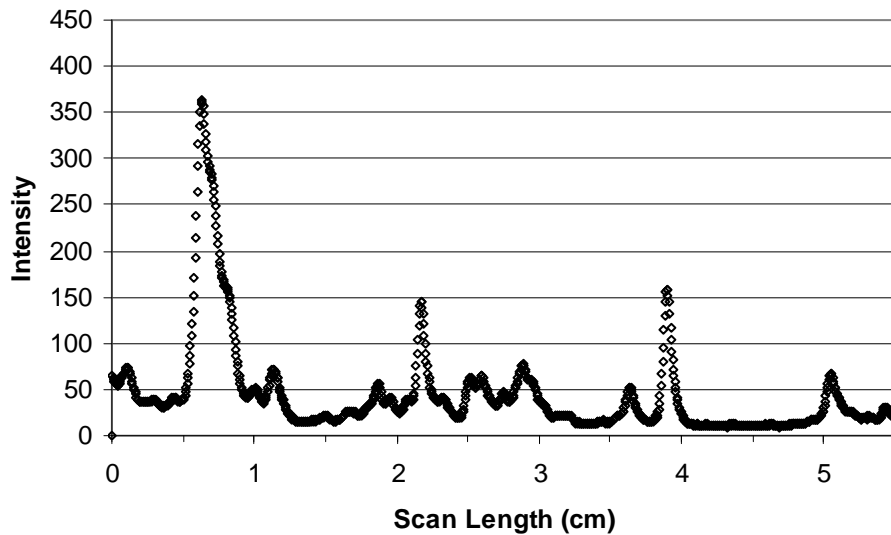


Figure III.32. Waveguide loss of sample spun coat at 2000 rpm and heated to 80°C; approximately 1 dB/cm.

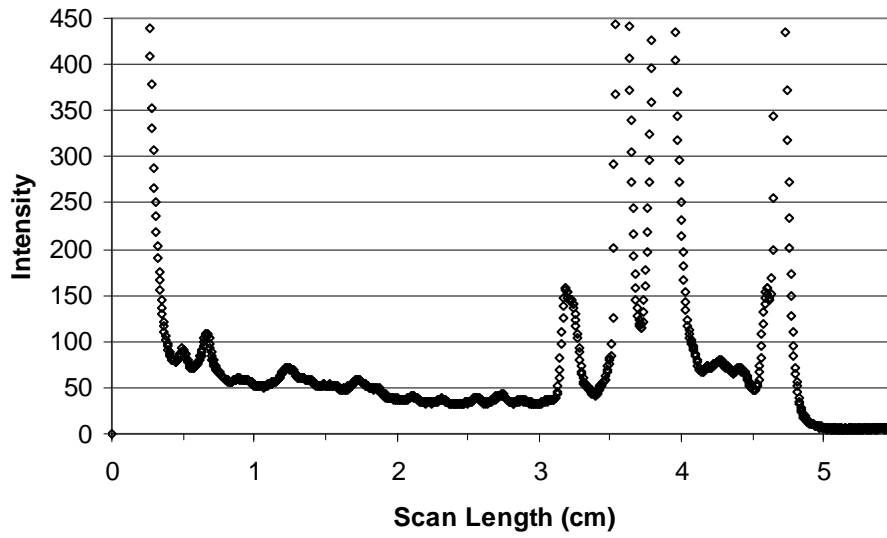


Figure III.33. Waveguide loss of sample spun coat at 2000 rpm and heated to 220°C; approximately 1.5 dB/cm.

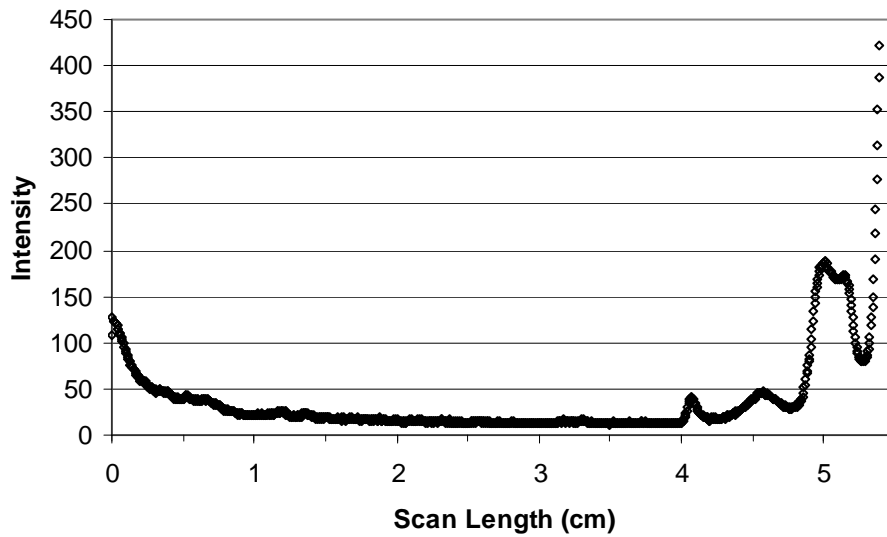


Figure III.34. Waveguide loss of sample spun coat at 2000 rpm and heated to 270°C; approximately 3 dB/cm.

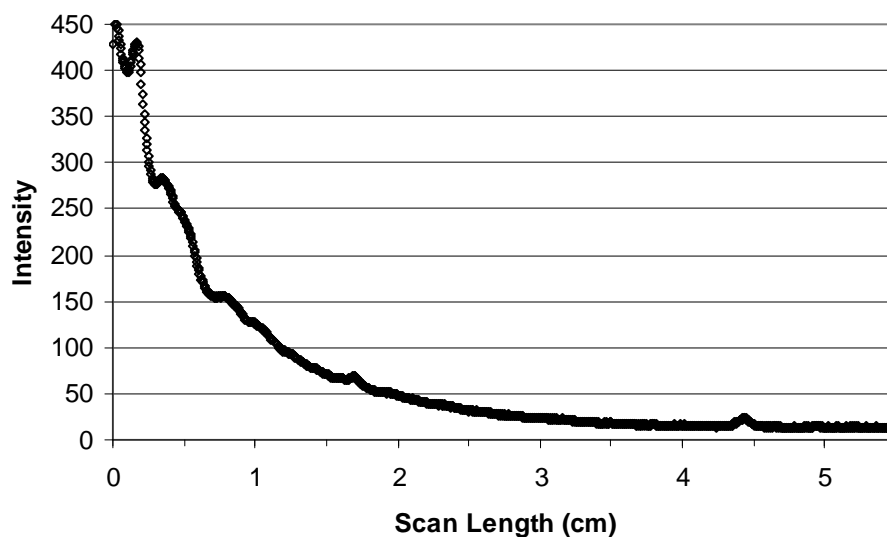


Figure III.35. Waveguide loss of sample spun coat at 2000 rpm and heated to 320°C; approximately 15 dB/cm.

The results of these measurements are given in Figure III.36. The loss of the low temperature gel film appears to be dominated by extrinsic defects. The baseline of the trace used to measure the loss is overwhelmed by scattering sites leaking the majority of the light. The baseline loss increases slightly as more solvent is driven off above 80°C. But it is not until temperatures exceed 250°C, when PVP decomposes, that the loss jumps to a very high value. Further measurements at higher temperatures exceed the detection limit of the prism coupler.

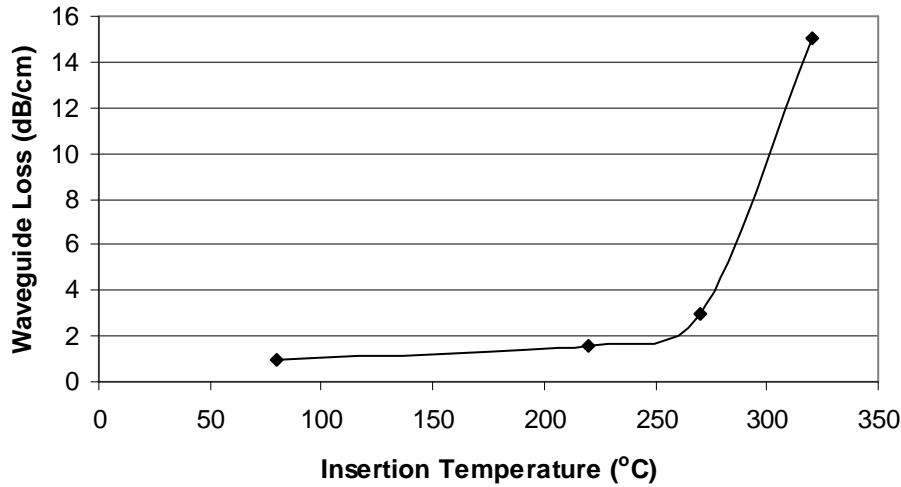


Figure III.36. Waveguide loss of film as a function of insertion temperature.

The primary loss mechanism in the thin films is scattering, which is a function of two main contributors: fluctuations in the refractive index and thickness. Index fluctuations are a volumetric effect, manifesting themselves as the dielectric misalignment of grains and other departure from a perfectly homogenous microstructure, such as porosity. Thickness fluctuation is an interfacial effect usually taking the form of film roughness.

Light scattering experiments and modeling by Sinclair and Dimos^{8,9} tell us that the fraction of power scattered per solid angle can be expressed by:

$$\frac{1}{P_0} \left(\frac{dP}{d\Omega} \right) = \gamma_{opt}^V \frac{|\Delta\epsilon(\vec{k})|^2}{L^2} \quad (16)$$

where γ_{opt}^V is the ‘optical coefficient’ and contains all information regarding thin film configuration, L^2 is the illuminated area and $\Delta\epsilon(\vec{k})$ is the two-dimensional Fourier

transform of the dielectric fluctuation autocorrelation function. Taking the case where the dielectric fluctuation correlation length is small compared to the wavelength of light, this autocorrelation function simplifies to:

$$\Delta\varepsilon(\vec{k}) = (\xi_0\tau_0)^2 \quad (17)$$

where ξ_0 is the amplitude of the fluctuations and τ_0 is the correlation length. In a polycrystalline microstructure the correlation length is limited to the grain, domain or crystal size. The dielectric fluctuation can be explained by recalling that the index of refraction is related to the dielectric constant. Therefore the maximum fluctuation amplitude is related to the birefringence of the material. A similar model is used to express scattering of light due to thickness fluctuation:

$$\frac{1}{P_0} \left(\frac{dP}{d\Omega} \right) = \gamma_{opt}^s \frac{|z(\vec{k})|^2}{L^2} \quad (18)$$

where $z(\vec{k})$ is the two-dimensional Fourier transform of the surface topography. Just as a greater fluctuation in the dielectric constant will lead to a greater scattered intensity of light from the volume, greater surface roughness will lead to increased scattering by the surface.

This model explains some of the curious behavior noted in the previous sections. It was suggested by X-ray diffraction data that the crystal size may should have only a small some effect on the scattering behavior of these heated films. This model would have the scattered intensity go as the square of the crystal size. It also explains the

increase in waveguide loss with temperature. The as-deposited film is amorphous and the index of refraction is relatively homogenous. At 250°C when PVP begins to burn off, a discontinuous matrix is left behind and small domains or clusters of solid material form within the film. It is this microstructure that dictates the crystallization at higher temperature into the nano-sized crystals detected by X-ray diffraction.

G. Proposed Mechanisms

As the gel film is heated and transformed into a partially crystalline thin film, the various stages of the process are explained as follows. The sol is spun to form the film and is then immediately dried at 100°C. Unbound solvent is driven off from the matrix leading to a gelled network. The refractive index at this point is 1.56 (633 nm) and the thickness is dependent primarily on the spinning speed (Figure III.7). The propagation loss is low at this point, as there is little variability in the refractive index or roughness. Upon heating to 200°C, it is reasonable to believe that all the remaining solvent has been driven from the structure. The index and loss increase and thickness decreases slightly. At 300°C, the decomposition and combustion of PVP begins. The removal of this major component results in a steeper decrease in thickness due to a reactivated condensation process and collapse of the network. The index continues to increase due to densification.

It is at this point that the loss of the film is sharply higher due to both scattering and absorption. Absorption occurs due to formation of polymer sub-species during decomposition of the PVP. The carbon dangling bonds invariably present in the products of decomposition lead to discoloration and absorption of light. This is one mechanism for the loss. However, as PVP constitutes only a small fraction of the overall mass, this is likely not the dominant mechanism. As the PVP is removed from the matrix, it leaves behind a discontinuous metal-oxide network. Small nanosized metal-oxide clusters are formed separated from others by void space that constitutes the spatial fluctuation in the composite dielectric constant. The formation of these clusters also leads to a surface

roughness of appreciable magnitude. Because the film is bound at the interface with the cladding, shrinkage occurs primarily in one (z) direction, leaving the film-air interface with an enhanced roughness compared to the as-coated film

The thickness variance, together with the dielectric fluctuation in the bulk, broadens the guiding modes and leads to increased scattering.

At 400°C the decomposition of PVP is expected to be complete and partial removal of acetate groups in the matrix has occurred. The loss is high, still attributable to scattering and possibly absorption. Heat treatment to 500°C sees the removal of all remaining organic species from the matrix. There does not appear to be that great of a change in thickness compared to 400°C, but the index does continue to increase due to the onset of crystallization. Loss continues to be high, but the mechanism is entirely scattering at this point. The band gap of BaTiO₃ is sufficiently high that no intrinsic absorption should take place by the bulk. At 600°C no new processes have begun, but the crystallization process continues. There is a nominal change in index and thickness. At 700°C the film is continuing to crystallize accompanied by nominal change in index and thickness. However, further heat treatment is still necessary to fully crystallize the film. Step-heating the film to 500°C then 700°C generates the highest index and consolidates the film to roughly 25% of its initial thickness. Despite the crystalline nature of the film at this point and the drastic reduction in volume, the refractive index of the film is still considerably lower than the average bulk value, 2.46. The obvious explanation for this is persistent nano-porosity remaining in the structure, although this is against expectations. The nano-crystalline microstructure locked in during organic

removal is highly scattering due to the surface roughness of the film, residual porosity and the intrinsic birefringence of the BaTiO₃ crystallites.

IV SUMMARY AND CONCLUSIONS

Electro-optic films with low loss are of renewed interest as advancements in the field of planar lightwave circuits provide a ripe opportunity for integrated circuits with active elements. Given the wide spread of loss values for propagation of light through such films, barium titanate was used as a model system to study light attenuation through the film.

Barium titanate sol containing a large polymeric additive was used to deposit thin films ($\sim 0.3 \mu\text{m}$) on silica clad silicon wafers. It is known that the ketone groups in the polymer form hydrogen bonds to with the hydroxyl sites in the metalloxane network. This structure increases the viscosity and lowers the polycondensation of the sol-gel allowing for crack-free deposition of thicker gel films. A para-linear dependence on spinning speed was determined for the dried gel thickness as measured by prism coupling. Using prism coupling data and X-ray diffraction, it was determined that faster heating rates produce films of higher index and smaller crystallites.

Analysis of the films as they were heated shows the anticipated trends: decreasing thickness and increasing refractive index. Thermal analysis of the sol reveals the temperatures at which various components of the sol gel matrix decompose and/or combust and helps validate the trends in film properties. The increase in waveguide loss with processing temperature can be explained using this thermal analysis data. The loss of the gel films was desirably low; approximately 1 dB/cm. This is attributable to the continuous, amorphous, non-absorbing gelled network within the film. Between the temperatures of 250° and 350°C , the large polymeric additive, polyvinylpyrrolidone, is

removed. The discontinuous matrix left behind is highly scattering due to dielectric fluctuation between isolated regions of nanosized metal-organic clusters. At this point, this microstructure of optically scattering nanodomains is locked into the microstructure, preventing transmission of light through the film.

At temperatures exceeding 500°C, all organic materials matter is believed to be removed from the matrix. Crystallization of the perovskite phase begins, presumably seeded by the amorphous clusters in the microstructure. Further heat treatment at 700°C allows the film to crystallize completely. X-ray diffraction indicated these films were perovskite barium titanate with no apparent pyrochlore, as desired. This results in consolidation of the films to a quarter of its previous volume and an increase in refractive index. Curiously, the index is still lower than the bulk value. Scattering of the light in the film is very high due to surface roughness and the polycrystalline microstructure despite nanocrystals. It is proposed that the clusters of these nanocrystals with interspersed porosity cause a superimposing microstructure that leads to high scattering. This mechanism is increasingly evidenced in other systems with nanosized moieties highlighting the need to consider the macroscale effects when making analysis of optical phenomenon.

V FUTURE WORK

Prism Coupling at 1550nm

Current analysis of film properties is restricted to 633 nm. Further study of the films at 1550 nm would be desirable for direct application to communications systems. The prism coupler is equipped with a port allowing the installation of another source laser. Addition of this measurement would validate the measurements made at 633 nm and provide a better idea of the material behavior for practical application.

Spectroscopic Ellipsometry

Analysis of the films using spectroscopic ellipsometry would provide an independent confirmation of the thickness and index to the prism coupling data. Using a spectroscopic method, the refractive index and extinction coefficient for the thin film could be measured over a broad spectrum. Models of the mesostructure would also include surface interfacial regions and surface roughness layers. This would provide a more complete picture of the multi-layer structure.

High-Resolution Microscopy

Difficulty imaging the films arose due to the fine scale of the features. Crystallite sizes of nanometer scale were far too small to resolve using the scanning electron microscopes available. Surface features disappeared under the thin layer of metal sputtered onto the surface during sample preparation. Edge saturation effects obscured the thin film in fracture surface images. The recently acquired electron microprobe would allow higher

resolution imaging of sample microstructure. Transmission electron microscopy of the films would also provide a confirmation of the crystal size at different stages of heat treatment.

Surface Roughness Characterization

Surface roughness is an important, and often dominant, contribution to scattering in thin films. In the place of atomic force microscopy, Zygo Interferometry may be used to characterize the surface roughness of the films. This information can be directly related to scattering measurements and modeling.

Spectrally Resolved Light Scattering

The use of polycrystalline thin films as waveguides requires the minimization of light loss. This requires an in-depth understanding and control of the scattering mechanisms. By studying the response of light scattering to processing variables, we may optimize the microstructure to application quality.

BaTiO₃ Dispersed in a Glass Matrix

To explore the role the individual clusters in light scattering, crystalline BaTiO₃ could be suitably dispersed in a glass matrix. This would avoid clusters of nanoparticles behaving as scattering elements.

Eliminating Porosity

Future use of sol-gel derived thin films in optical applications requires optimized microstructure. Further study of processing is required to understand the role of porosity in the films. By eliminating porosity from the material, scattering loss ought to be decreased and the effective index of the film will more closely approximate the bulk value.

Templated Oriented Grain Growth

Another method of optimizing the microstructure requires the use of templated grain growth. MgO substrates, for example, have been shown to selectively orient the BaTiO₃ thin film with a c-axis columnar microstructure due to their closely-matched lattice parameters. This enhanced microstructure may provide better film properties and lower scattering loss. Recent work at the University of Illinois reports the growth of epitaxial Sr_{0.5}Ba_{0.5}TiO₃ using a fluorinated acetic acid solution and firing in a dry atmosphere.

REFERENCES

1. Handbook of Optics, Vol. IV, *Fiber Optics and Nonlinear Optics*, 2nd ed.; pp. 57-60; Ch. 4. Edited by M. Bass. McGraw-Hill, 2001.
2. S.O. Kasap, *Optoelectronic Devices and Photonics: Principles and Practices*; Ch. 7. Prentice-Hall, Upper Saddle River, New Jersey, 2001.
3. M. Sugiyama, M. Doi, S. Taniguchi, T. Nakazawa, and H. Onaka, "Driver-less 40 Gb/s LiNbO₃ Modulator with Sub-1 V Drive Voltage," pp. FB61-4 in, *OFC 2002: Optical Fiber Communication Conference and Exhibit: Technical Digest*. Optical Society of America, Washington, D.C.
4. M.E. Lines and A.M. Glass, *Principles and Applications of Ferroelectrics and Related Materials*; Ch. 13. Oxford University Press, New York, New York, 1977.
5. A.M. Glass, "Optical Materials," *Science*, **235** [4792] 1003-9 (1987).
6. G.H. Haertling and C.E. Land, "Hot-Pressed (Pb,La)(Zr, Ti)O₃ Ferroelectric Ceramics of Electrooptic Applications," *J. Am. Ceram. Soc.*, **54** [1] 1-11 (1971).
7. M.H. Garret and I. Mnushkina, "Techniques for Top-Seeded Solution Growth of BaTiO₃," *J. Cryst. Growth*, **166** [1-4] 550-7 (1996).
8. M.B. Sinclair, D. Dimos, B.G. Potter, and R.W. Schwartz, "Light Scattering from Sol-gel Processed Lead Zirconate Titanate Thin Films," *Int. Ferroelectrics*, **7** [1-4] 225-36 (1995).
9. M.B. Sinclair, D. Dimos, B.G. Potter, R.W. Schwartz, and C.D. Buchheit, "Light Scattering from Sol-Gel Pb(Zr,Ti)O₃ Thin Films: Surface versus Volume Scattering," *Int. Ferroelectrics*, **11** [1-4] 25-34 (1995).
10. Materials Research Society Symposium - Proceedings, Vol. 597, *Thin Films for Optical Waveguide Devices and Materials for Optical Limiting*. Edited by N. Nashimoto, B.W. Wessels, J. Shmulovich, A.K.-Y. Jen, K. Lewis, R. Pachter, R. Sutherland, and J. Perry. Materials Research Society, Warrendale, PA, 1999.
11. R.A. McKee, F.J. Walker, E.D. Specht, and K.B. Alexander, "MBE Growth and Optical Quality of BaTiO₃ and SrTiO₃ Thin Films on MgO," pp. 309-14 in Materials Research Society Symposium - Proceedings, Vol. 341, *Epitaxial Oxide*

Thin Films and Heterostructures. Materials Research Society, Pittsburgh, PA, 1994.

12. C. Buchal, L. Beckers, A. Eckau, J. Schubert, and W. Zander, "Epitaxial BaTiO₃ Thin Films on MgO," *Mater. Sci. Eng. B*, **56** [2-3] 234-8 (1998).
13. J.G. Lisoni, M. Siegert, C.H. Lei, W. Biegel, J. Schubert, W. Zander, and C. Buchal, "The Growth of MgO Buffer Layers on Sapphire for the Epitaxy of BaTiO₃ Optical Thin Films," *Thin Solid Films*, **389** [1-2] 219-26 (2001).
14. M. Siegert, J.G. Lisoni, C.H. Lei, A. Eckau, W. Zander, C.L. Jia, J. Schubert, and C. Buchal, "Epitaxial BaTiO₃ Thin Films on Different Substrates for Optical Waveguide Applications," pp. 145-50 in Materials Research Society Symposium - Proceedings, Vol. 597, *Thin Films for Optical Waveguide Devices and Materials for Optical Limiting*. Materials Research Society, Warrendale, PA, 2000.
15. L. Beckers, W. Zander, J. Schubert, P. Leinenbach, C. Buchal, D. Fluck, and P. Gunter, "Epitaxial BaTiO₃ and KNbO₃ Thin Films on Various Substrates for Optical Waveguides Applications," pp. 549-54 in Materials Research Society Symposium - Proceedings, Vol. 441, *Thin Films - Structure and Morphology*. Materials Research Society, Pittsburgh, PA, 1997.
16. A. Petraru, M. Siegert, M. Schmid, J. Schubert, and C. Buchal, "Ferroelectric BaTiO₃ Thin Film Optical Waveguide Modulators," pp. 279-84 in Materials Research Society Symposium - Proceedings, Vol. 688, *Ferroelectric Thin Films X*. Materials Research Society, Warrendale, PA, 2002.
17. Y. Nakata, G. Soumagne, T. Okada, and M. Maeda, "Pulsed-Laser Deposition of Barium Titanate Films and Plume Dynamics," *Appl. Surf. Sci.*, **127-129** [May 1] 650-4 (1998).
18. D.-Y. Kim, S.E. Moon, E.-K. Kim, S.-J. Lee, J.-J. Choi, and H.-E. Kim, "Electro-optic Characteristics of (001)-Oriented Ba_{0.6}Sr_{0.4}TiO₃ Thin Films," *Appl. Phys. Lett.*, **82** [9] 1455-7 (2003).
19. V.N. Koinkar and S.B. Ogale, "Pulsed Excimer Laser Processing of Optical Thin Films," *Thin Solid Films*, **206** [1-2] 259-63 (1991).
20. F. Tcheliobou, H.S. Ryu, C.K. Hong, W.S. Park, and S. Baik, "On the Microstructure and Optical Properties of Ba_{0.5}Sr_{0.5}TiO₃ Films," *Thin Solid Films*, **305** [1-2] 30-4 (1997).

21. Y.-M. Tsau, Y.-C. Chen, H.-F. Cheng, and I.-N. Lin, "Ferroelectric (Ba,Sr)TiO₃ and Pb(Zr,Ti)O₃ Thin Films Prepared by Pulsed Laser Deposition," *J. Eur. Ceram. Soc.*, **21** [10-11] 1561-4 (2001).
22. H.-F. Cheng, "Structural and Optical Properties of Laser Deposited Ferroelectric (Sr_{0.2}Ba_{0.8})TiO₃ Thin Films," *J. Appl. Phys.*, **79** [10] 7965-71 (1996).
23. D.H. Kim and H.S. Kwok, "Pulsed Laser Deposition of BaTiO₃ Thin Films and Their Optical Properties," *Appl. Phys. Lett.*, **67** [13] 1803-5 (1995).
24. B.W. Wessels, "Ferroelectric Oxide Epitaxial Thin Films: Synthesis and Non-linear Optical Properties," *J. Cryst. Growth*, **195** [1-4] 706-10 (1998).
25. F. Niu, A.R. Teren, B.H. Hoerman, and B.W. Wessels, "Epitaxial Ferroelectric BaTiO₃ Thin Films for Microphotonic Applications," pp. E191-E6 in Materials Research Society Symposium - Proceedings, Vol. 637, *Microphotronics - Materials, Physics and Applications*. Materials Research Society, Warrendale, PA, 2001.
26. D.M. Gill, B.A. Block, C.W. Conrad, B.W. Wessels, and S.T. Ho, "Thin Film Channel Waveguide Electro-optic Modulator in Epitaxial BaTiO₃ on MgO," p. 507 in Conference on Lasers and Electro-Optics Europe - Technical Digest, Vol. 11, *Proceedings of the 1997 Conference on Lasers and Electro-Optics*. IEEE, Piscataway, NJ, 1997.
27. G.M. Ford, A. Teren, and B.W. Wessels, "Luminescent Properties of Er-doped BaTiO₃ Thin Films for Optical Waveguides," pp. 101-6 in Proceedings of SPIE - The International Society for Optical Engineering, Vol. 3622, *Rare-Earth-Doped Materials and Devices III*. Society of Photo-Optical Instrumentation Engineers, Bellingham, WA, 1999.
28. D.M. Gill, G.M. Ford, B.A. Block, S.-S. Kim, B.W. Wessels, and S.T. Ho, "Guided Wave Absorption and Fluorescence in Epitaxial Er:BaTiO₃ on MgO," *Thin Solid Films*, **365** [1] 126-8 (2000).
29. A.R. Teren, S.-S. Kim, S.-T. Ho, and B.W. Wessels, "Erbium-doped Barium Titanate Thin Film Waveguides for Integrated Optical Amplifiers," pp. 413-8 in Materials Research Society Symposium - Proceedings, Vol. 688, *Ferroelectric Thin Films X*. Materials Research Society, Warrendale, PA, 2002.
30. S. Kim, S. Hishita, Y.M. Kang, and S. Baik, "Structural Characterization of Epitaxial BaTiO₃ Thin Films Grown by Sputter Deposition on MgO(100)," *J. Appl. Phys.*, **78** [9] 5604-8 (1995).

31. S. Kim and S. Hishita, "Growing BaTiO₃ Thin Films on Si(100) with MgO Buffer Layers by Sputtering," *Thin Solid Films*, **281-282** [1-2] 449-52 (1996).
32. S. Kim and S. Hishita, "Preparation and Characterization of BaTiO₃ Thin Films on MgO-Buffered Si(100) Substrates by RF Sputtering," *J. Mater. Res.*, **12** [4] 1152-9 (1997).
33. P. Barrios, C.C. Li, H.K. Kim, and J. Blachere, "Structural, Electrical and Optical Properties of Erbium-doped Epitaxial BaTiO₃ Films Grown by RF Sputtering," pp. 279-84 in Materials Research Society Symposium - Proceedings, Vol. 401, *Epitaxial Oxide Thin Films II*. Materials Research Society, Pittsburgh, PA, USA, 1996.
34. D.H. Cruz and R.A. Lessard, "BaTiO₃ Thin Films Fabricated by Sol-gel Process," pp. 9-16 in Proceedings of SPIE - The International Society for Optical Engineering, Vol. 4804, *Sol-Gel Optics VI*. The International Society for Optical Engineering, 2002.
35. P.C. Joshi and S.B. Desu, "Structural, Electrical, and Optical Studies on Rapid Thermally Processed Ferroelectric BaTiO₃ Thin Films Prepared by Metallo-Organic Solution Deposition Technique," *Thin Solid Films*, **300** [1-2] 289-94 (1997).
36. M. Manso-Silvan, L. Fuentes-Cobas, R.J. Martin-Palma, M. Hernandez-Velez, and J.M. Martinez-Duart, "BaTiO₃ Thin Films Obtained by Sol-gel Spin Coating," *Surf. Coat. Technol.*, **151-152** [Mar. 1] 118-21 (2002).
37. H.B. Sharma and A. Mansingh, "Sol-Gel Processed Barium Titanate Ceramics and Thin Films," *J. Mater. Sci.*, **33** [17] 4455-9 (1998).
38. S.H. Sharma, H.N.K. Sarma, and A. Mansingh, "Ferroelectric and Dielectric Properties of Sol-Gel Processed Barium Titanate Ceramics and Thin Films," *J. Mater. Sci.*, **34** [6] 1385-90 (1999).
39. I. Suzuki, M. Ejima, K. Watanabe, Y.-M. Xiong, and T. Saitoh, "Spectroscopic Ellipsometry Characterization of Ba_{0.7}Sr_{0.3}TiO₃ Thin Films Prepared by the Sol-gel Method," *Thin Solid Films*, **313-314** [1-2] 214-7 (1998).
40. H.Y. Tian, W.G. Luo, X.H. Pu, X.Y. He, P.S. Qiu, A.L. Ding, S.H. Yang, and D. Mo, "Determination of the Optical Properties of Sol-gel-derived Ba_xSr_{1-x}TiO₃ Thin Film by Spectroscopic Ellipsometry," *J. Phys.: Condens. Matter*, **13** [18] 4065-74 (2001).

41. H.-Y. Tian, W.-G. Luo, A.-L. Ding, J. Choi, C. Lee, and K. No, "Influences of Annealing Temperature on the Optical and Structural Properties of (Ba,Sr)TiO₃ Thin Films Derived from Sol-gel Technique," *Thin Solid Films*, **408** [1-2] 200-5 (2002).
42. H.-Y. Tian, W.-G. Luo, X.-H. Pu, X.-Y. He, P.-S. Qiu, and A.-L. Ding, "Synthesis and Dielectric Characteristic of Ba_{1-x}Sr_xTiO₃ Thin Films-based Strontium-Barium Alkoxides Derivatives," *Mater. Chem. Phys.*, **69** [1-3] 166-71 (2001).
43. X. Xiang, L. Hou, and F. Gan, "Sol-gel Derived BaTiO₃ Thin Films," *Vacuum*, **42** [16] 1057-8 (1991).
44. H. Kozuka and A. Higuchi, "Stabilization of Poly(vinylpyrrolidone)-containing Alkoxide Solutions for Thick Sol-gel Barium Titanate Films," *J. Am. Ceram. Soc.*, **86** [1] 33-8 (2003).
45. H. Kozuka and M. Kajimura, "Single-step Dip Coating of Crack-free BaTiO₃ Films >1μm Thick: Effect of Poly(vinylpyrrolidone) on Critical Thickness," *J. Am. Ceram. Soc.*, **83** [5] 1056-62 (2000).
46. H. Kozuka and A. Higuchi, "Single-layer Submicron-thick BaTiO₃ Coatings from Poly(vinylpyrrolidone)-containing Sols: Gel-to-ceramic Film Conversion, Densification, and Dielectric Properties," *J. Mater. Res.*, **16** [11] 3116-23 (2001).
47. R. Ulrich and R. Torge, "Measurement of Thin Film Parameters with a Prism Coupler," *Appl. Opt.*, **12** [12] 2901-8 (1973).
48. B. Jaffe, W.R.J. Cook, and H. Jaffe, *Non-Metallic Solids*, Vol. 3, *Piezoelectric Ceramics*; Ch. 5. Academic Press, New York, 1971.
49. R. Jenkins and R.L. Snyder, *Chemical Analysis*, Vol. 138, *Introduction to X-ray Powder Diffractometry*; pp. 89-91; Ch. 3. John Wiley & Sons, New York, 1996.